Holocene relative sea-level changes and coastal evolution along the coastlines of Kamaran Island and As-Salif Peninsula, Yemen, southern Red Sea

Ahmed Saif Al-Mikhlafi[(1),] Fiona D. Hibbert[(2)], Lawrence R. Edwards[(3)], Hai Cheng[(3)]

(1) Department of Earth and Environmental Sciences, Sana'a University, Sana'a, Republic of Yemen

(2) Research School of Earth Sciences, The Australian National University, Canberra, ACT 2601, Australia

(3) Department of Earth Sciences, University of Minnesota, Minneapolis, MN 55455. USA.

Corresponding author: Ahmed Saif Al-Mikhlafi (ahmed.almikhlafi@fulbrightmail.org; ahmedmikhlafi@hotmail.com)

Abstract

Geomorphic features (fossil terraces, notches and sea cliffs) from the southern Red Sea coasts provide valuable indicators of past sea-level change that enable the quantification of both the timing and magnitude of the mid-Holocene sea-level highstand. We demonstrate the utility of wave-cut notches in the southern Red Sea, and present U-series dated sea-level indicators from two locations on the As-Salif Peninsula that suggest a mid-Holocene highstand of ~ 0.5 to 1 m above present mean sea level (apmsl) at about 5 to 5.4 ka BP. In addition, the similarity of the elevations of the different sea-level indicators at the two locations in As-Salif Peninsula and Kamran Island suggest relative tectonic stability, with limited influence of salt diapirism. Comparison of our data to other estimates of the Red Sea mid-Holocene highstand, and glacio-isostatic predictions suggest that water loading (and deformational response) is the primary factor in the spatial and temporal variability the mid-Holocene highstand, with some possible localized tectonic and neotectonic overprinting.

Key words:

Red Sea; mid-Holocene sea level; coastal geomorphology; fossil corals; wave-cut

notches; U-series dating

1. INTRODUCTION

Relatively little is known about the relative sea level (RSL) variations during the Holocene for large segments of the Red Sea coasts, especially the south of the basin (e.g., Edelman-Furstenberg et al., 2001; Lamy et al., 2006; Lambeck et al., 2011). Early studies assigned emerged sea-level indicators (e.g., coral terraces) along the Red Sea coast to sea-level fluctuations and tectonic processes only, and ignored contributions from the glacio-isostatic adjustment (GIA) and water loading processes (e.g., Al-Rifaiy and Cherif, 1988; Gvirtzman et al., 1992; El-Asmar, 1997; Strasser and Strohmenger, 1997; Shaked et al., 2002). As GIA affects not just near-field regions (i.e., those located close to the former ice sheets) but also the intermediate and locations such as the Red Sea (Mitrovica and Peltier, 1991; Peltier, 1999; Milne and Mitrovica, 2008; Lambeck et al., 2014), considerable spatial variability in amplitude, magnitude and timing of highstands in the Red Sea is expected and predicted from GIA modelling (Lambeck et al., 2011).

Tectonically, the Red Sea is not stable and geologic, geodetic and seismic evidence indicates pronounced vertical movements across the Red Sea basin throughout the latest rifting phase that started in the Miocene (Girdler and Styles, 1974; Hötzl, 1984; Hempton, 1987; Purser and Bosence, 1998). In addition, vertical movement associated salt diapirism occurs in some parts of the Red Sea, such as the As-Salif Peninsula (Figure 1) and these vertical movements have influenced the carbonate reef deposits, often resulting in irregular uplift of the terraces.

As indicators of local sea level form as a result of the interplay between eustatic sea-level change, tectonic uplift or downwarping, and GIA processes, we expect the combined imprint of each of these processes to be preserved at the stratigraphic record of the Red Sea. In this study we utilize wave-cut notches from the southern Red Sea, Kamaran Island and the As-Salif Peninsula, to provide information on both local tectonic history and past sea level. We provide mid-Holocene coral U-series ages for the Yemeni Red Sea coast and document geomorphic features on As-Salif

Peninsula and Kamaran Island coasts. We take advantage of the varied geologic/ neotectonic setting of the area to: (i) investigate the potential of wave-cut notches as a palaeo tide and sea-level indicators in the Red Sea; (ii) provide sea-level constraints to test the GIA predictions of Red Sea sea levels during the Holocene; and (iii) interpret the tectonic history of the complex, faulted region in the southern Red Sea.

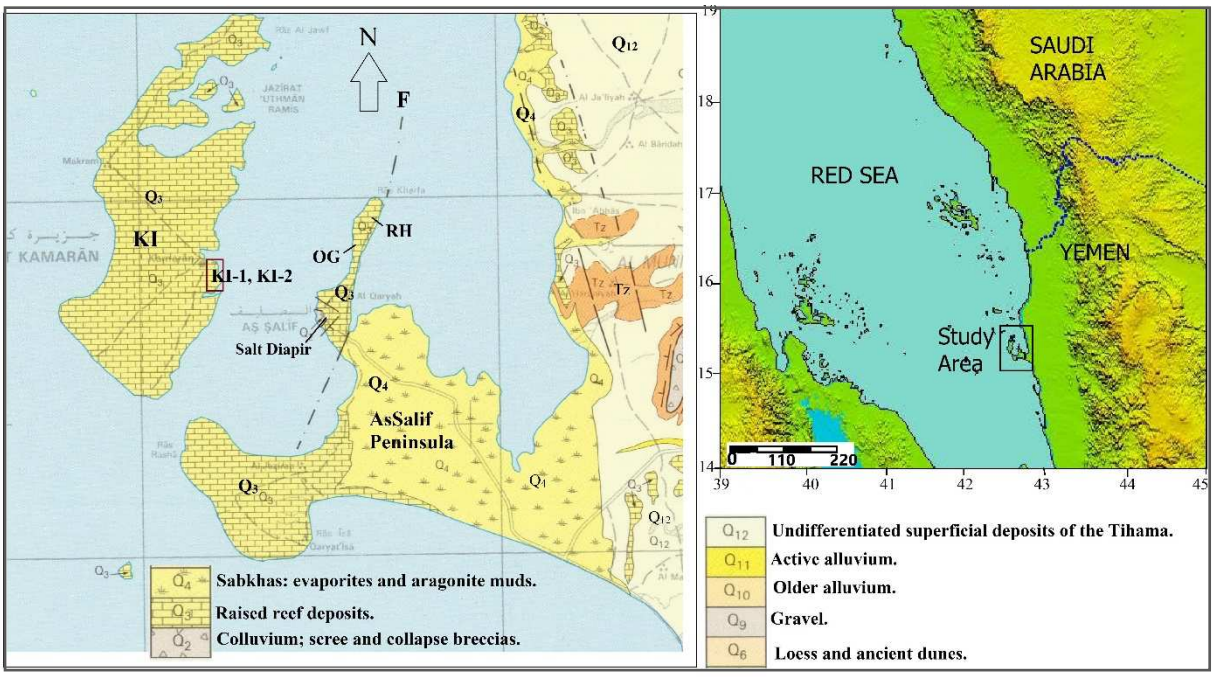

Figure 1: Topographic map of Yemeni Red Sea showing Kamaran and As-Salif Peninsula and the study/sampling locations (OM = Om Gedi; RH = Ras Harafa; KI-1 and KI-2 are the two sampling locations on Kamaran Island).

2. LOCATION, GEOMORPHOLOGY AND STRATIGRAPHY

2.1 Tidal regime and coastal setting

The Red Sea is characterized by a semi-diurnal microtidal regime, with the tidal range increasing with distance from the centre of the basin, from virtually no daily change to about 0.6 m in the north and up to 0.9 m in the south (at Massawa and Kamaran Island) (Edwards, 1987). The tidal range results from the interaction of tides produced in the Red Sea itself and the co-oscillation with the Indian Ocean (Defant, 1961). The latter is attenuated by the narrow Bab al Mandeb Strait resulting

in generally low tidal amplitudes in the Red Sea. The effect of the strait can be seen from increasing tidal amplitudes northwards, with the highest tidal range recorded in Kamaran Island of ~ 1 m.

The wave regime (direction, wave height) at the study sites is driven by three principal seasonal wind systems operating in the Red Sea, and waves tend to propagate along the axis of the Red Sea basin (Clifford et al., 1997; Sofianose, 2003; Langodan et al., 2017). Significant wave height varies seasonally with the monsoon reversal (Ralston et al., 2013; Langodan et al., 2018); during the winter, monsoon winds from the southeast generate waves with mean significant wave heights in excess of 2 m and mean periods of 8 s in the southern Red Sea, with lower wave heights during the summer (Ralston et al., 2013). The indented coasts of the Red Sea leads to a reduction in swell, especially in the southern zone (Langodan et al., 2017).

2.2 As-Salif Peninsula

The As-Salif Peninsula is part of the ~40 km wide, N-S trending, Tihama coastal plain (Davison et al., 1994) (Figure1). The southern Red Sea, including islands and volcanic coastal formations, are associated with the main Red Sea Rift and Afar rift, which are parallel to the coast and have numerous fault lines (Rowlands and Purkis, 2015). An irregular distribution of carbonate bodies occurs as a result of local faults, differential uplift due to salt diapirs, and variable erosion/depositional processes (Bosence, 2005; Purkis et al., 2012; Rowlands and Purkis, 2015). Tectonically, the As-Salif Peninsula is an intensely deformed area, with vertical bedding and steeply plunging isoclinal folds (Davison el al., 1996).

The geomorphology of Red Sea makes it conducive to evaporite and salt diapir formation (Bosworth, 2015) with mid- to late Miocene salt deposits (16.4-5.3 Ma) forming shortly after Red Sea basin rifting terminated (Heaton et al., 1996; Davison et al., 1996). The vast desert and arid climate of the region also create the conditions for salt diapirs to form and develop into domes and islands (Bosence, 2005). The evaporites in this region are sandwiched between Pliocene siliciclastics sediments

beneath, and Pleistocene and Holocene carbonates above (Brown, 1970; Mitchell et al., 1992; Bosence et al., 1998). The stress exerted by the rocks above, force the evaporites to elevate the overlaying strata to create diapiric structures (Purser and Bosence, 1998; Bosence et al., 1998; Gracia et al., 2008).

The As-Salif Peninsula is produced by a linear north-south trending salt diapir, bounded by a normal growth fault on the eastern margin, and this diapiric wall continues offshore for several kilometres (Bosence et al., 1998). Boreholes drilled in the region show that evaporite influence is unevenly distributed beneath the coastal shelf, and the thickest evaporites are found offshore (Bosence et al., 1998; Rowlands et al., 2014). The domed morphology of As-Salif diapir is topped by corals dominated by *Galaxea fascicularis*, particularly in the lower sections of the fossil reefs, with more diverse coral assemblage in the upper section of the reefs (Bosence, 2005; Purkis and Riegl, 2012) (Figure 2).

In brief, the Salif Formation in the region comprises a thick halite, disconformably overlain by bedded gypsum with thin layers of carbonate (the Ghawwas Member), capped by about 5 m of gypsiferous/calcareous clastics. The Salif Formation is intermittently exposed along the coastal region of the Tihamah plain of the Yemeni Red Sea and we selected two emergent terraces for further investigation. These comprise two low lying, flat-topped emergent terraces in the northern As-Salif Peninsula, Om Gedi and Ras Harafa (Figure 1). A normal fault, which is oriented parallel to salt diapir faults, passes through the northernmost As-Salif Peninsula, and may be responsible for the emergence of these terraces (Rowlands and Purkis, 2015).

The Om Gedi terrace (OG) (upper Salif Formation), is formed predominantly of coarse to fine grained siliciclastic lithology impregnated with gypsiferous/anhydrite beds (Figure 3). Such deposits are typically a result of sabkha cycles, where alternating episodes of sea water saturation and flushing with meteoric water in intertidal sediments lead to gypsum formation (Wright, 1994). The high content of siliciclastic grains suggests deposition by wind (Youssef, 1991).

The Ras Harafa terrace (RH) is largely formed of gypsum and gypsiferous clastics intercalated with detrital material (also upper Salif Formation) (El-Nakhal and Alaug, 2013; Beydoun et al., 1998), with a series of cliffs, notches, and caves on its seaward face. Recent gypsum deposits encrust coral reef fragments atop a wave-cut platform below to marine terrace (Figure 4). The shape and location of the As-Salif Peninsula terraces suggests a primary tectonic control on their spatial distribution.

2.3. Kamaran Island

Kamaran Island (KI) is located in shallow waters of north-eastern part of Yemeni Red Sea and separated from the eastern coast by a narrow strait known as As-Salif strait (Figure 1). The island is a post-rift sequence formed of carbonate deposits that developed on the eroded uppermost layer of the Plio-Pleistocene platform (Angelucci, 1981; Angelucci et al., 1985). These carbonate deposits (reefal limestones, ca. 1.81 - 0.01 Ma) represent the uppermost 10 m of a shallow water sedimentary complex that overlies an evaporite sequence of Miocene age (Davison et al., 1996; Bosence et al., 1998).

A sequence of notches, cliffs, and platforms is evident in the carbonate rocks of Kamaran Island. These were incised through tidal and/or wave action and can be used as a palaeo-sea level indicators, although debate as to the exact processes governing formation continues (e.g., Pirazzoli, 1986; Rust and Kershaw, 2000; Kershaw and Guo, 2001; Kelletat, 2005; Evelpidou et al., 2012; Moses, 2013). Recent sediments comprise mostly of fossil remains (e.g., corals, molluscs, calcareous algae, and benthic foraminifera) and reworked materials from the nearby rocks.

3. MATERIALS AND METHODS

We mapped the geomorphic features (wave-cut notches, cliffs etc.) at each site; elevations were determined using either direct measurement by levelling and/or differential Global Positioning System (GPS) measurements and are reported relative to present mean sea level (above present mean sea level, apmsl). The uncertainty in the GPS elevation measurement is ± 2 cm, with greater uncertainty associated with

our levelling (we use a conservative estimate of 20 %). The inflection points of wave-cut notches indicates the position of mean sea level at the time of formation (Antonioli et al., 2015). However, we had difficulty in determining the vertex at our sites, as most of the notches are of U-shape and/or obscured by sediment. As such, we report the approximate elevation of the inflection point through comparison with analogue modern notches. The total elevation error was calculated by summing all the contributing sources of error in quadrature (Table 1).

We collected *in situ Porites* sp. and *Acropora* sp. corals (i.e., the corals were found upright in growth position, with no indication of later displacement) for U-series dating. We assume corals from the fossil reef platform immediately below the wave-cut notches lived at the time as when the notch was cut (cf. Rovere et al., 2015; Lorscheid et al., 2017). Modern corals in the area are intertidal. Twelve coral samples were collected (Table 1): 6 samples from two locations in Kamran Island (KI01 and KI02) (at +4 ± 1 m apmsl), two *in situ* corals from a patch reef on top of the As-Salif diapirs (+18 ± 2 m apmsl); two *in situ* corals from the Om Gedi (OG) (+1 ± 0.2 m apmsl) and; two corals *in growth* position from Ras Harafa (RH) (+ 0.5 ± 0.2 m apmsl) (Figure 1).

Corals selected for radiometric dating were initially examined petrographically and by X-ray diffraction to ensure that corals were primary aragonite. The XRD determinations were carried out using Rigaku Miniflex XRD, with JADE 7 software (Connolly, 2010) used for peak identification. All corals collected from the As-Salif peninsula terraces are pristine (i.e., < 2 % calcite), whereas the coral samples from Kamaran Island were diagenetically altered (i.e., recrystallized) and only two samples from Kamaran Islands with the least amount of alteration (visual appearance and % calcite) were U-series dated. Samples that passed the initial XRD screening were lightly crushed and any discoloured material and/or debris was removed using a binocular microscope. Coral samples were then quarried out into cubes followed by multiple ultrasonic baths in distilled water, and dried at 30^{o}C. The chemical procedures for the separation of U and Th from the sample are based on methods of Edwards et al. (1987). Approximately 0.2 - 0.3 g of ultrasonically cleaned samples

were weighed and spiked with a mixed ^{229}Th-^{233}U-^{236}U tracer. Uranium and thorium were separated with iron co-precipitation and anion-exchange chromatography. The uranium and thorium aliquots were dissolved in 1% HNO_3 + 0.005N HF for instrumental measurements (Shen et al., 2002). Samples were subsequently analyzed by Neptune multi-collector inductively coupled plasma mass spectrometer (MC-ICP-MS) and a Faraday-multiplier following the procedure developed by Edwards et al. (1987, 1988); Cheng et al. (2008) and Shen et al. (2002). Ages were calculated using a half-life for ^{230}Th of 75,690 years and a half-life for ^{234}U of 245,250 years (Cheng et al., 2013). The age was solved for iteratively using the standard age equation presented in Edwards et al. (1987), using decay constants of 1.55125 x10^{-10} for λ_{238} (Jaffey et al., 1971), 2.82206 x 10^{-6} for λ_{234} (Cheng et al., 2013), and 9.1705 x10^{-6} for λ_{230} (Cheng et al., 2013). In addition, samples were corrected for initial non-radiogenic thorium using a ^{230}Th/^{232}Th atomic ratio of 4.4 ± 2.2 x10^{-6}.

4. RESULTS

4.1 U-series dating

Five *in situ* coral samples were collected from As-Salif Peninsula (two from the top of As-Salif Salt diapir, two from Ras Harafa (RH), and one from Om Gedi (OG). The measured ^{238}U concentrations of our samples varies between 1.14 and 2.61 ppm (Table 1). Samples from RH have ^{238}U concentrations consistent to modern pristine corals of living/dead corals from Bab al-Mandab (Al-Mikhlafi et al., 2018), and modern corals from Red Sea (Friedman, 1968; Gvirtzman et al., 1973). However, Holocene corals from the Om Gedi and As-Salif salt diapir have lower ^{238}U concentrations (Table 1), suggesting that these corals may have experienced secondary elemental or isotopic disturbance (cf. Yu and Zhao, 2010). The concentration of ^{232}Th in our samples varies from 0.375 ± 0.009 to 1.59 ± 0.033 ppb, the latter is significantly above the 0.5 ppb of pristine corals from oceanic islands and likely reflects the incorporation of detrital material into the corals (Edwards et al., 1987; Chen et al., 1991; Yokoyama et al., 2001). The modern value of $\delta^{234}U_i$ is widely used to detect digenetic alteration of fossil corals (e.g., Bard et al., 1991; Hamelin et al., 1991; Gallup et al., 1994) and all samples except those from Kamaran Island have calculated $\delta^{234}U_i$ values that are similar to the modern seawater value (146.8 ± 1 ‰,

Andersen et al., 2010).

Table 1. U-series data of samples from Kamaran Island and As-Salif peninsula, southern Red Sea. All uncertainties are reported at the 2 sigma uncertainty level.

Sample/ Species	Elev. (m)	^{238}U (ppm)	^{232}Th (ppb)	$^{230}Th/^{232}Th$ (atomic x10^{-6})	$\delta^{234}U^{*}$ (meas.)	$^{230}Th/^{238}U$ (activity)	^{230}Th Age (yr) (uncorrected)	^{230}Th Age (yr) (corrected)	$\delta^{234}U_{initial}$** (corrected)	^{230}Age (yr BP)*** (corrected)
Bab El-Mandab: Living or modern-dead corals collected from ~2 m b.s.l near to Perim Island (AL-Mikhlafi et al., 2018).										
BM01 *Porites* sp.	-2±0.5	2.14 ±0.002	0.0401±0.004	78.4±93.9	146.4±1.2	0.0001±0.0001	8±10	8±10	146 ±1	-53±10
BM02§ *D. strigosa*	-2±0.5	2.72 ±0.003	0.1827±0.005	28.8±20.5	146.9±1.3	0.0001±0.0001	11±8	9±80	147±1	-52±80
BM03 *Porites* sp.	-2±0.5	2.09 ±0.003	0.8469±0.018	13.8±3.3	144.5±1.5	0.0003±0.0001	32±8	22±11	145±2	-41±11
Note: BM 01 and 02 are different samples (new collections), BM 03 is from different location (old collections)										
As Salif (Holocene corals)										
OG01 *Porites* sp.	1.0±0.2	1.21±0.0015	1.42±0.0291	727.9±15.1	144.2±1.5	0.0518±0.0002	5043±21	5013±30	146±2	4950±30
RH01 *Acropora* sp.	0.5±0.2	2.61±0.005	1.5865±0.0333	1528.0±34.1	142.1±2.5	0.0562±0.0004	5500±46	5485±47	144±3	5423±47
RH02 *Acropora* sp.	0.5±0.2	2.48±0.0049	0.8766±0.0185	2575.9±55.2	143.6±2.1	0.0553±0.0002	5395±24	5386±25	146±2	5324±25
SL01 *Porites* sp.	18±2	1.42±0.0019	0.3749±0.0092	4866.0±120.4	147.3±1.8	0.0782±0.0002	7685±26	7679±26	150±2	7616±26
SL02 *Porites* sp.	18±2	1.14±0.0015	1.4823±0.0307	999.5±20.9	146.7±1.8	0.0787±0.0003	7744±29	7711±38	150±2	7648±38
Kamaran Island (old fossil corals)										
KI01 *Porites* sp.	4±1	0.74 ±0.0008	4.1605±0.0836	2728.7±55.0	50.3±1.5	0.9303±0.0016	226636±1871	226485±1871	95±3	226422±1871
KI02 Faviidae	4±1	0.62 ±0.0009	8.123±0.1631	1054±21	-23.7±2.2	0.8437±0.0017	222169±2528	221766±2533	-44±4	221703±2533

U decay constants: $l_{238} = 1.55125x10^{-10}$ (Jaffey et al., 1971) and $l_{234} = 2.82206x10^{-6}$ (Cheng et al., 2013). Th decay constant: $l_{230} = 9.1705x10^{-6}$ (Cheng et al., 2013).
*$d^{234}U = ([^{234}U/^{238}U]_{activity} - 1)x1000$. ** $d^{234}U_{initial}$ was calculated based on ^{230}Th age (T), i.e., $d^{234}U_{initial} = d^{234}U_{measured} \times e^{l_{234}xT}$.
Corrected ^{230}Th ages assume the initial $^{230}Th/^{232}Th$ atomic ratio of 4.4 ±2.2 x10^{-6}. Those are the values for a material at secular equilibrium, with the bulk earth $^{232}Th/^{238}U$ value of 3.8.
The errors are arbitrarily assumed to be 50%
***B.P. stands for "Before Present" where the "Present" is defined as the year 1950 A.D.
The tidal range in Kamaran Island is ~1 m, and datum is taken as 0.5 m.
§ living corals.

All samples (except Kamaran Island) are mid-Holocene in age (after correction for detrital thorium, Table 1); samples from the top of the As-Salif salt diapir (SL01 and SL02) are dated to 7,616 ± 26 and 7,648 ± 38 years BP; Ras Harafa samples (RH01 and RH02) have ages of 5,423 ± 47 and 5,324 ± 25 years BP; and the Om Gedi coral sample was dated to 4,950 ± 30 years BP. The two fossil corals collected from Kamaran terraces were diagenetically altered with almost complete transformation from pristine aragonite skeleton into calcite. These samples yielded ages of 226,422 ± 1,871 years and 221,703 ± 2,533 years BP, although the dates obtained are unlikely to reflect the 'true' age of these samples due to the significant diagenetic alteration.

4.2 Reef and notch morphology

4.2.1 Al-Salif Peninsular salt diapir

Patch corals were found at altitude of +18 ± 2 m (apmsl) atop of As-Salif salt diapir (Figure 2) and two coral samples (*Porites* sp.) yielded mean (inverse weighted) age of 7,629 ± 31 years BP (Table 1). These samples were dated to confirm the Holocene age of this reef and investigate local deformation due to salt diapirism. Although

these samples passed initial XRD screening (i.e., calcite content of < 2%), further investigation suggests U-depletion in both samples (SL01 and SL02). Further, sample SL02 has elevated ^{232}Th concentration compared to modern equivalents indicative of detrital input (see section 5.1 for further discussion of the age of these samples).

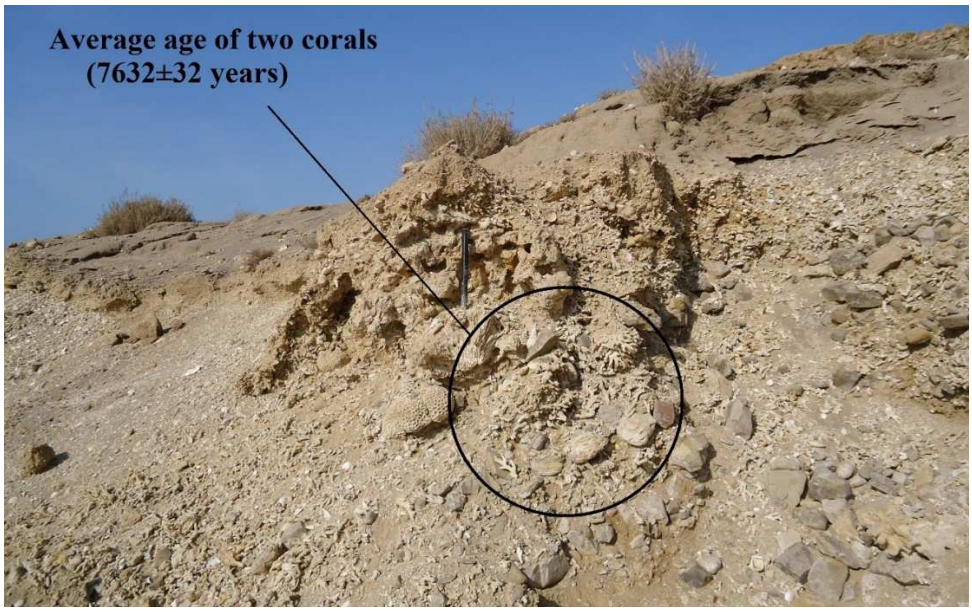

Figure 2: Coral samples (SL01 and SL02, circled) from the As-Salif salt diapir.

4.1.2 Om Gedi terrace (OG)

The OG terrace has a maximum mapped elevation of + 4 ± 1 m apmsl. It comprises an indurated aeolian (continental source) deposit, overlain by gypsiferous layer. Inspection of the OG terrace siliciclastic beach rocks indicate deposition in relatively quiet, subaerial and oxygen rich environment (fine grains and yellowish staining of the indurated sediments). The lack of reef corals at this site (i.e., the reefal limestone that overlies the Salif Formation elsewhere on the Kamaran and As-Salif Peninsula) may be due to very high terrestrial inputs and turbid-water environment that is unfavorable for large-scale carbonate production (Purser et al., 1987). A wave-cut notch mapped at +3 ± 1 m apmsl (Figure 3) and is assumed to be of Last Interglacial (LIg) age. We were unable to obtain reliable date for this feature but have assign a Last Interglacial age given the proximity and similarity in elevation to the U-series dated fossil reef at Bab al-Mandab, southern Red Sea (4±1 m apmsl; Al-Mikhlafi et al., 2018). This notch has its middle and upper portions preserved as notch roof,

292 whereas its base buried under the aeolinite sand. A Holocene cliff developed below
293 the LIg notch at an elevation of ~+1.5 m (Figure 3). An *in situ Porites* sp. coral (OG1;
294 +1 ± 0.2 m apmsl), found intercalated with siliciclastic deposits adjacent to the
295 Holocene wave-cut cliff, was dated to 4,950 ± 30 years BP (Table 1), and considered
296 equivalent in age to cliff formation (Figure 3). The shape of Holocene cliff suggests
297 that the cliff developed initially in the cohesionless aeolinite material and that the
298 roof collapsed, likely due to wave action.
299

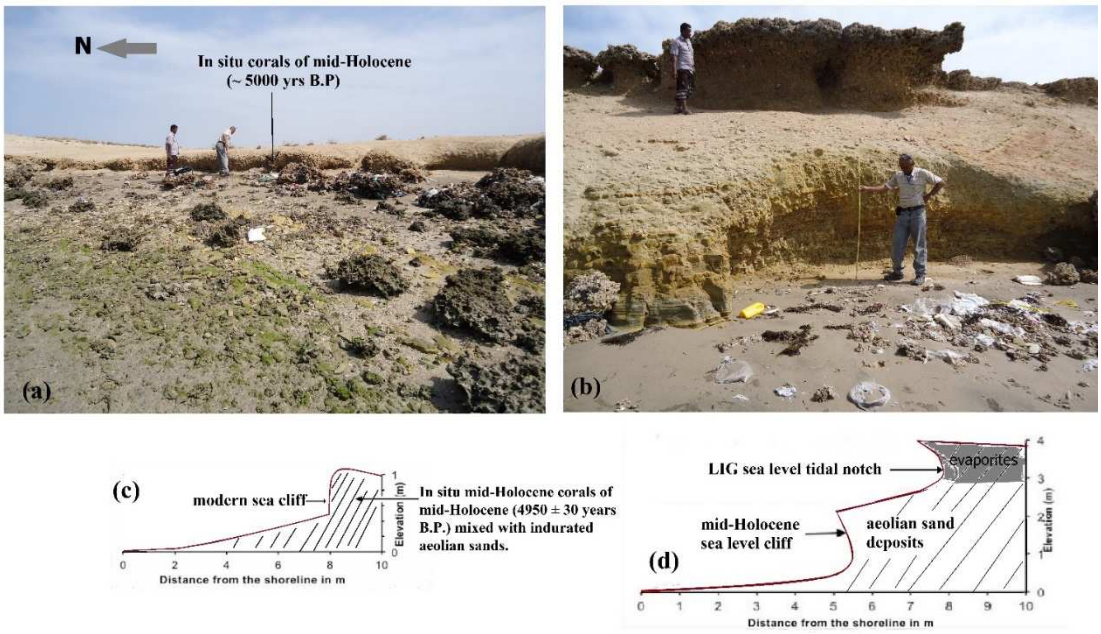

Figure 3: Photographs and field sketches of the Om Gedi terrace, As-Salif Peninsula. (a) An outcrop of *in situ Acropora* sp. of mid-Holocene age capped by siliciclastic sediments; and in the foreground, reworked boulder of gypsiferous sandstone from the main terrace (b) Photograph of mapped stratigraphic sequence showing mid-Holocene abrasion notch, with overlying LIg notch; (c) cross-section of (a) and; (d) cross-sections of (b).

300 *4.1.3 Ras Harafa (RH)*
301 RH is the northernmost terrace of As-Salif peninsula, and is the uppermost part of
302 the Salif Formation. It has a maximum elevation of +3 ± 1 m apmsl. The terrace is
303 formed of gypsum/gypsiferous clastics intercalated with fine grained siliciclastic

material, with gypsum deposits (likely sabkha). Again, the reef limestones that typically overlie the Salif Formation are not represented here. Notches and solutional caves (Figure 4b), which can indicate the position of sea level at the time of their formation (Mylroie and Carew, 1988; Florea et al., 2007), are cut into the late-Miocene terrace (Figure 4c). Patch corals of Holocene age (RH01 and RH02; both +0.5 ± 0.1 m apmsl, Table 1) were found in a modern lagoon setting below the RH terrace at elevation of ~ 0.5 m apmsl. Recent gypsum deposits with mushroom/stromatolites morphologies are found encrusting mid-Holocene patch corals and are emerged during low tide (Figure 4a).

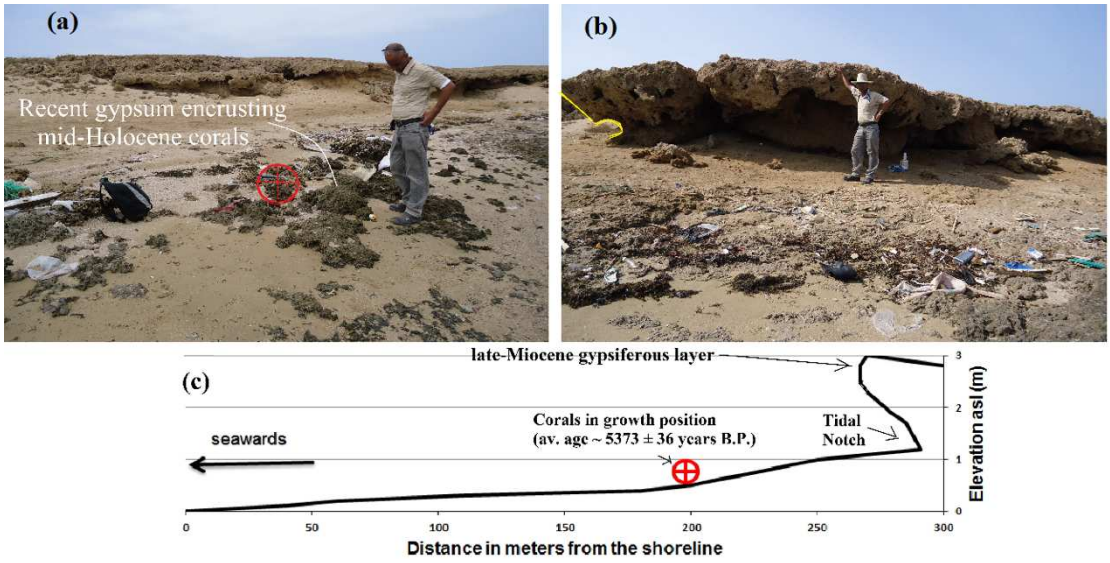

Figure 4: The Ras Harafa terrace, As-Salif Peninsula. (a) photograph of Holocene corals (foreground) with samples RH01 and RH02 highlighted in red. Assumed late-Miocene age terrace in the background; (b) notches/solution caves cut into late-Miocene terrace; (c) schematic cross-section of the Ras Harafa terrace.

4.1.4 Kamaran Island (KI)

The Kamaran Limestone is capped with a compact and highly weathered reef carbonate of early Pleistocene age, and contains variety of well-developed notches, and cliff structures. The area is microtidal and has generally sheltered coastal sites making the area promising for sea-level reconstruction.

In the north of the island, we documented distinct asymmetrical V-shaped notches with inflection points of 0.5 ± 0.2 m apmsl (Figure 5). The eastern part of Kamaran

Island is influenced by localized (neotectonic) vertical movement of the salt diapir intrusion, with clear displacement in the elevation of surveyed geomorphic features (reverse fault evident in Figure 6a). Five sites in this location were mapped in detail. At the first site, an embryonic notch (i.e., modern) is forming at close to present sea level in the Holocene cliff (maximum elevation ~ 1 ± 0.2 m apmsl) (Figure 6b, see also map in the *Supplementary Information doi: 10.6084/m9.figshare.13079240*). At the second location (slightly to the north), a series of notches was mapped, with 4 notches at elevations ranging from approximately +4 m to +2 apmsl (Figure 7a and b). This 'staircase' morphology (i.e., vertical separation of the notches) and U-shaped geometry (i.e., widening and deepening) of these notches likely resulted from vertical motion associated with coseismic uplift associated with the As Salif salt diapir (cf. Schneiderwind et al., 2017).

Progressing further around the bay to the north, a well-developed U-shaped notch of assumed LIg period is found at elevation of ~3 ± 1 m apmsl in weathered marly limestone (Figure 8a) and a V-shaped notch is well defined at +0.5 ± 0.2 m apmsl. Neither of these notches were dated but based on their elevation and comparison with other sites in the region, we assign the upper to the LIg and the lower to the mid-Holocene. *Lithophaga* boreholes in the lower unit may suggest slow uplift subsequent to the LIg period.

Finally, a well-developed, symmetric V-shaped wave-cut notch was observed in the uppermost section of the terrace, and corals at ~ +3 ± 1 m apmsl were selected for dating to corroborate our assumption of LIg age for notches cut at the elevation at this site (Figure 8b). Unfortunately, these corals were all highly diagenetically altered (corals KI01and KI02, Table 1) and yielded ages of >200,000 years BP (Table 1).

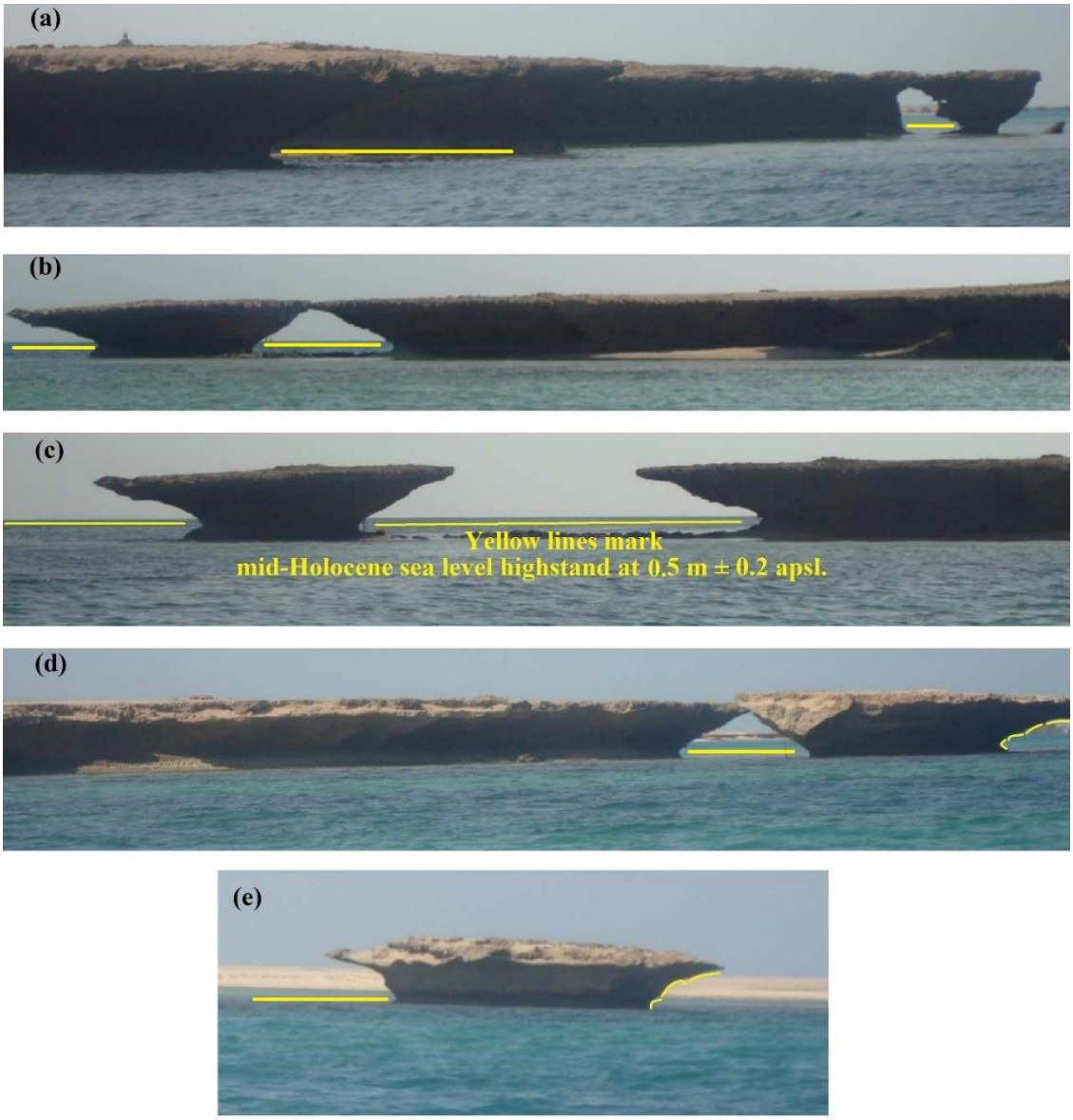

Figure 5: Wave-cut notches from the northern Kamaran Island, southern Red Sea. (a), and (b) were formed by wave action on a headland; (c), (d) and (e) sea stacks ("mushroom rocks") with well-developed marine notches just above present sea-level, and clear indentation at 0.5 m ± 0.2 apmsl.

347

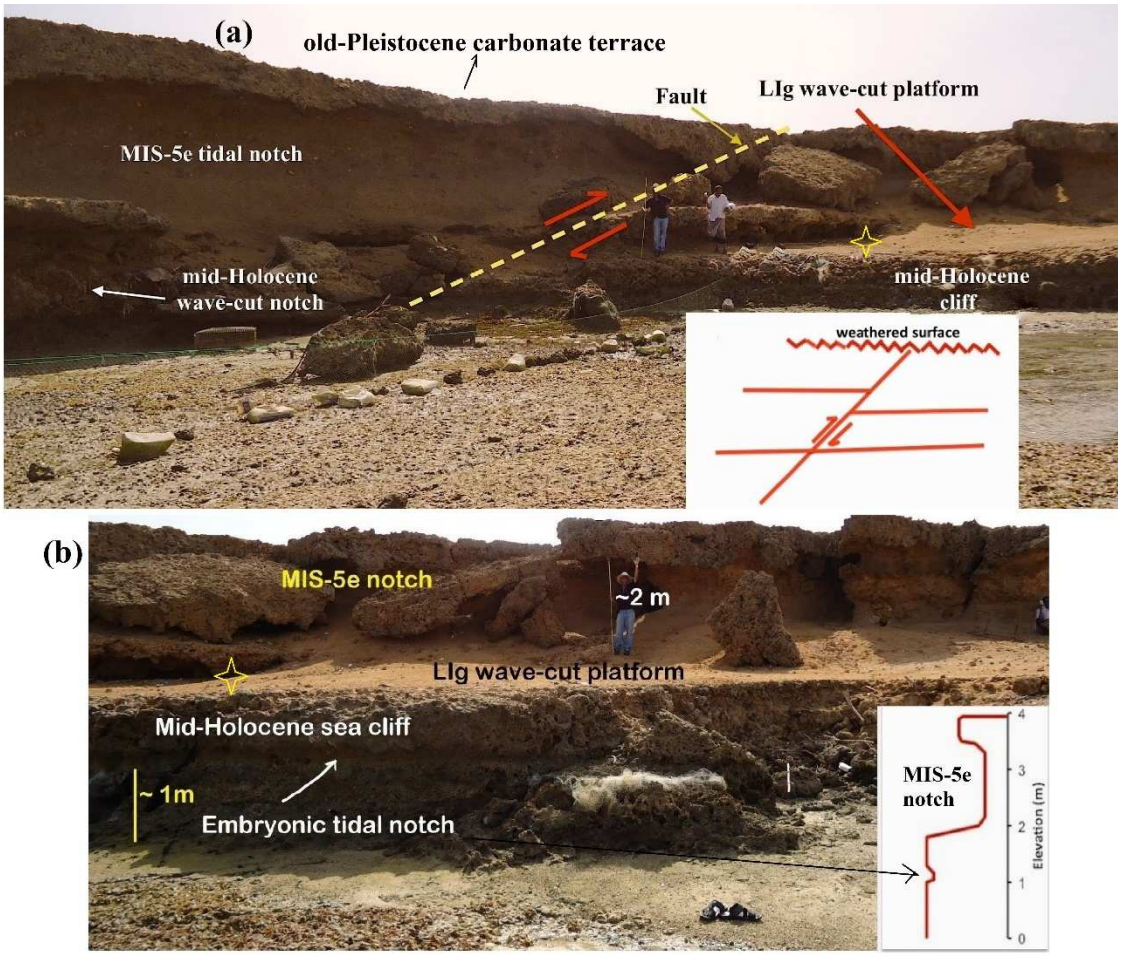

Figure 6: Photographs and schematic cross-sections of assumed reverse fault, eastern Kamaran Island. (a) observed reverse fault likely caused by neotectonics (schematic cross section, below right); (b) section to the right of yellow star in (a) which remained stable, showing the mid-Holocene wave-cut cliff and embryonic (modern) notch (schematic cross section, below right).

348

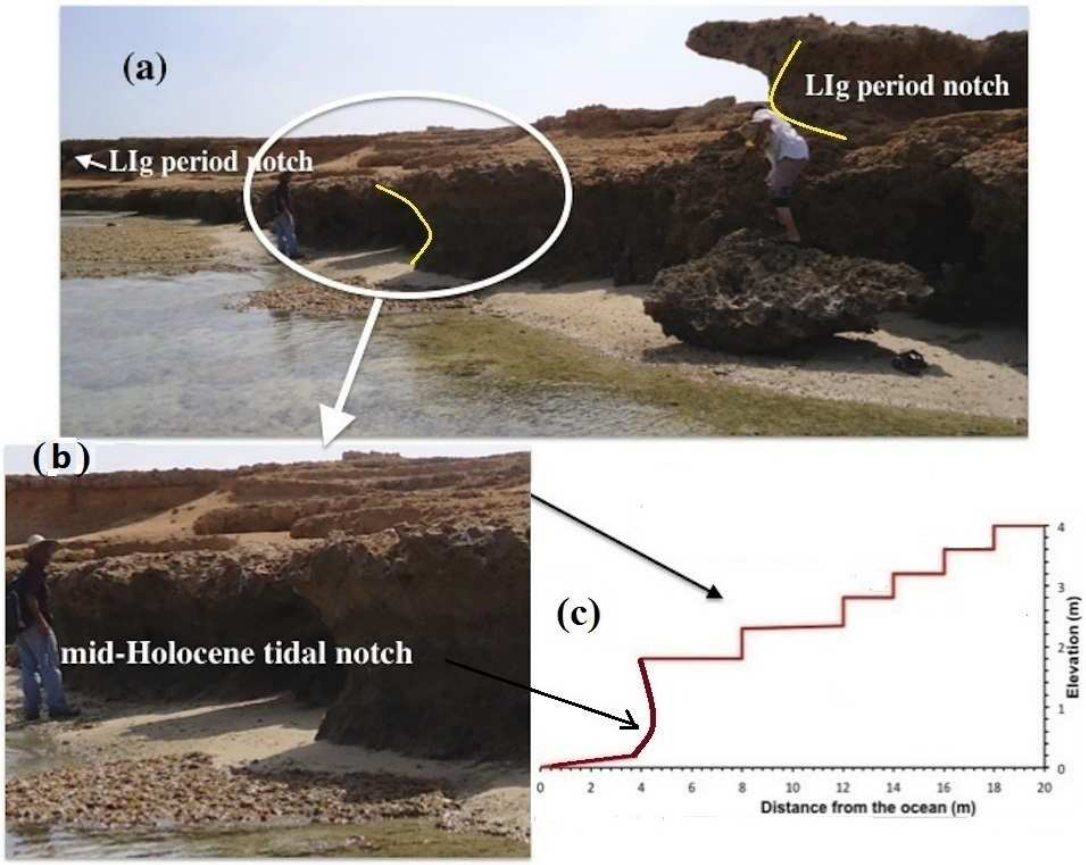

Figure 7: (a) Pleistocene carbonate terrace with a series of wave-cut features or sea-level oscillations ("staircase") of assumed LIg age (b) is a close up of the mid-Holocene notch; (c) schematic cross-section.

349

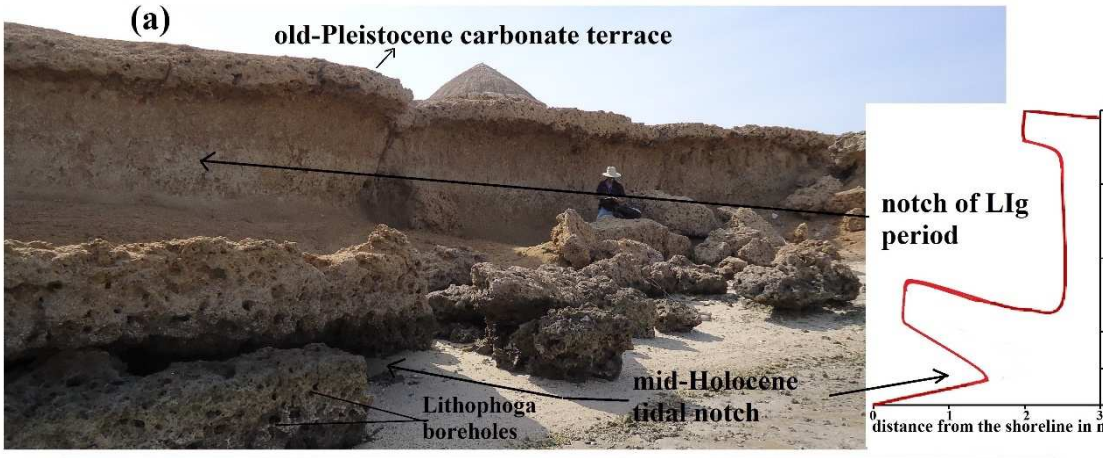

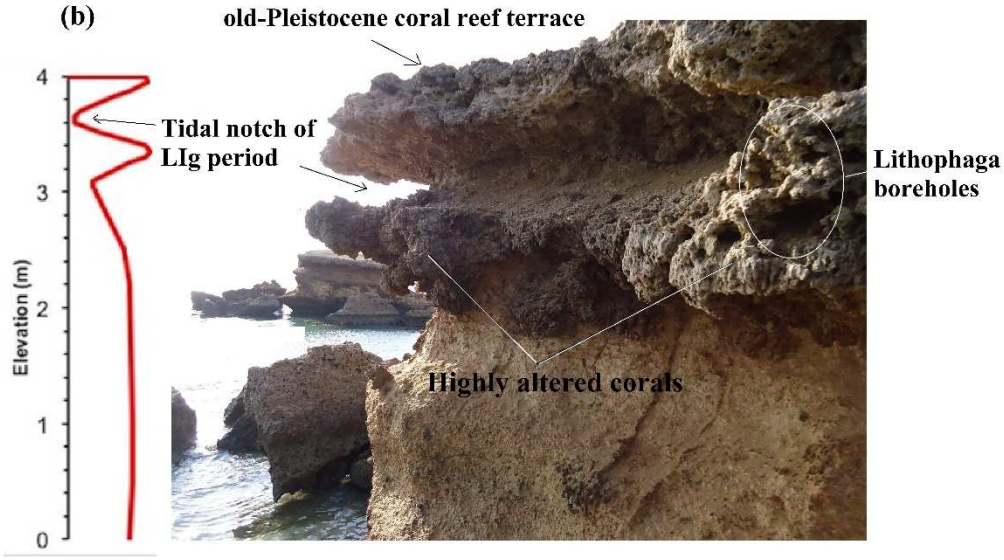

Figure 8: Pleistocene terrace with a U-shape of LIg wave-cut notch and V-shaped mid-Holocene wave-cut notch at ~ 0.5 ± 0.2 m below (schematic cross-section, right). (b) notch (assumed LIg age) cut into highly altered old-Pleistocene coral reefs at ~3±1 m apmsl.

5. DISCUSSION

5.1 Reliability of U-series geochemical data

All samples from this study show measured $(^{234}U/^{238}U)_{act}$ close to the modern sea water value of ~1.147 (Stirling and Andersen, 2009), and plot on or near the seawater evolution curve. All samples, except for those from RH, have ^{238}U and ^{232}Th concentrations that deviate from the live/dead corals of Bab al-Mandab (Al-Mikhlafi et al., 2018), modern corals from Aqaba (Scholz et al., 2004), and in the minimum range of ^{238}U concentrations of modern corals from Red Sea (~ 1.3 - 4.2 ppm) (Hibbert et al., 2016, and references therein) (Table 1). Plotting ^{238}U concentrations versus $(^{230}Th/^{238}U)$ activity ratios (Figure 9a) provides insights into the effect of uranium loss on the apparent ages, due to the inverse relationships between ^{238}U concentrations and $(^{230}Th/^{238}U)$ activity. Similarly, plotting ^{232}Th concentrations versus $(^{230}Th/^{238}U)$ activity ratio, suggest that the effect of any uranium loss was accompanied by thorium addition (Figure 9b). These changes probably resulted from post depositional uranium loss, moving the data to the right on the diagram without affecting $(^{234}U/^{238}U)$ activity (Figure 9c).

366

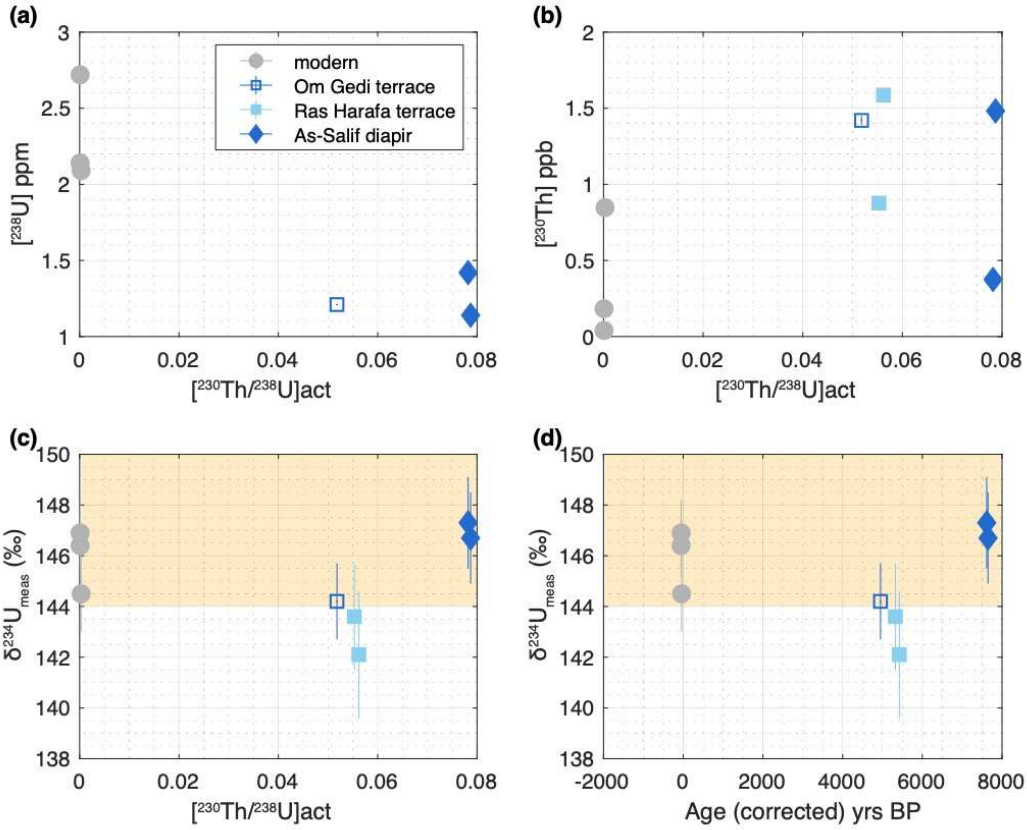

Figure 9: Bivariate plots of (**a**) ^{238}U concentration vs. $(^{230}Th/^{238}U)_{act}$ of samples from As-Salif Peninsula (note, errors are smaller than the symbols); (**b**) ^{230}Th concentration vs. $(^{230}Th/^{238}U)_{act}$ of the same samples (note, errors are smaller than the symbols); (**c**) Plot of $(\delta^{234}U)_{meas}$ vs. $(^{230}Th/^{238}U)_{act.}$ (**d**) $(\delta^{234}U)_{meas}$ vs. age of samples from the As-Salif Peninsula. The pale orange boxes represents the 'strictly reliable' values of $\delta^{234}U$ for modern seawater ($\delta^{234}U_{initial}$ = 147 ± 3 ‰). Errors are plotted at 2 sigma.

367 The corals from the top of the As-Salif salt diapir yielded mean U-series ages of
368 ~7,630 years BP. These ages are in contrast to conventional radiocarbon dates of
369 *Tridacna* shells by Davison et al. (1996) (reported as conventional radiocarbon ages
370 of 3,700 ± 250 and 3,850 ± 250 years) from the same site and elevation. Our samples
371 have lower ^{238}U concentrations than typical dead/live corals (2-3 ppm) and one,
372 SL02, also has high ^{232}Th content (i.e., above the 0.5 ppb value for pristine coral
373 samples), which may indicate the presence of secondary contamination. Both ^{238}U

374 loss and ^{232}Th high would increase the age and account for the offset with the
375 radiocarbon ages of the *Tridacna* shells.
376
377 **5.2 Notches as sea-level indicators in the southern Red Sea**
378 Abrasion by wave and currents can create permanent wave-cut notches that, if
379 preserved, can be useful palaeo sea-level indicators. Notches manifest as
380 indentations or undercuts of a few centimetres to several meters (Antonioli et al.,
381 2017) and form at or near mean sea level, during (a) prolonged stand-stills, and/or
382 (b) when the rates of erosional processes are in line with the pace of relative sea-
383 level change (Antonioli et al., 2006; Evelpidou et al., 2012). They are formed via
384 chemical dissolution processes, wetting and drying cycles, biological erosion, wave
385 action, or more likely, a combination of these factors (Antonioli et al., 2015). Often
386 their vertical extension almost equals the tidal range (e.g. Pirazzoli, 1986). As a
387 result, notches can serve as accurate sea-level indicators, especially in tectonically-
388 stable regions (Neumann and Hearty, 1996; Antonioli et al., 2006; Hearty et al.,
389 2007; Rodríguez-Vidal et al., 2007). However, in tectonically stable settings, wave-cut
390 notches that were created in the late Pleistocene can be reoccupied and modified in
391 the late-Holocene by sea level and associated wave action that reach similar
392 elevations (Phillips, 1970; Trenhaile, 1972; Kelsey, 1990; Kelsey and Bockheim,
393 1994). Notches can also form from other (often interrelated) processes including
394 eustatic/isostatic sea-level adjustments, tectonic and seismic processes (Carobene,
395 2015), as well as the action of chemical, physical, and biological factors (Pirazzoli,
396 1986, Antonioli et al., 2015).
397
398 A major limitation of using wave-cut notches as sea-level indicators is the difficulty in
399 directly dating their formation. The dating of organisms that form the biological rim
400 covering part of the notch (Pirazzoli et al., 1994a; Pirazzoli et al., 1994b; Faivre et al.,
401 2013) or correlating the elevation of a notch with other datable markers has proved
402 fruitful. An alternative approach, which we adopt here, assumes dates from corals
403 found on the platform immediately below the notch are coeval with notch formation
404 (Lorscheid et al., 2017). Unfortunately, we were unable to obtain ages for the older
405 notches (elevation ~3 to + 4 m apmsl) as the corals showed significant diagenetic

406 alteration and were unsuitable for dating. We therefore assume all notches at
407 approximately +4 m apmsl that directly overlie the mid-Holocene notches, date to
408 the LIg.
409
410 For the sites investigated, we found that some terraces are better preserved and less
411 eroded than others, and this is mainly dependent on the rock lithology and hydraulic
412 regime at each site. Sheltered beaches are more likely to develop notches than
413 beaches with aggressive hydraulic regime. We attribute the differences in
414 preservation/morphology of the features mainly to variation in tectonic activity of
415 the region, resistance of the rock, the time the rocks were exposed to wave attack,
416 and the variable occurrence of structural discontinuities such as cracks, fissures,
417 joints, bedding planes, and faults (cf. Lorscheid et al., 2017). Variations in
418 morphology (height, depth and shape) of the modern and fossil notches may also
419 arise if the rate of erosion is not gradual and continuous (cf. Pirazzoli and Evelpidou,
420 2013), or from exposure to sub-aerial weathering by coseismic activity (Stiros et al.,
421 2009, Pedoja et al., 2014).
422
423 At the tectonically stable Ras Harafa (RH) site, the sea cliff has a pronounced
424 cave/large notch at + 2 ± 1 m apmsl (inferred LIg age) which may have been
425 reoccupied during the late Holocene (Figure 10). This may suggest negligible GIA-
426 induced net relative sea-level change from one highstand to the next (LIg and
427 Holocene) and/or limited influence of tectonics, including salt diapirism in the area.
428

Figure 10: Photograph of the Ras Harafa terrace with LIg notch/cave at ~+2 ± 1 m apmsl; the yellow line is the highest tidal range.

In contrast, the preserved notch and sea cliff cut into the OG terrace, which is located closer to the As-Salif salt diapir, are distinctly separated in elevation (notches at ~+3 ± 1 m of inferred LIg age, and a mid-Holocene sea cliff at +1±0.2 m) (Figure 3b), with differences in host rock lithology having a strong control on their morphology. The LIg notch is carved into evaporite rocks, whereas the modern sea cliff is cut into poorly cemented recent aeolinite sand deposits. The LIg notch has additional structure, with middle and upper notch roofs preserved. The notch floor, however, is buried under aeolinite sand deposit making it difficult to measure the notch height, but this is clearly greater than the maximum modern tidal range. This could be a consequence of greater tidal range during the LIg, or a sequence of stillstands. The late Holocene sea cliff developed at the toe of LIg notch and probably formed as the result of abrasion processes where sediment entrained in waves or in turbulent broken wave bore, rushes up the beach face, excavating a "basal notch" and leaving the overhanging cliff material undermined, leading to failure (Bird, 2000). This process is promoted by the presence of groundwater in the cliff material (May and Heeps, 1985) and bioerosion (Trenhaile, 1987).

On Kamaran Island, a series of geomorphic structures - fossil coral terraces, wave cut platform, notches, and sea cliffs (Figure 6) – record past sea-level changes. A Holocene sea cliff is cut into indurated Pleistocene carbonate rocks at elevation of 1 ± 0.2 m apmsl. This has a composite structure with an embryonic notch forming at modern sea level (Figure 6b). The embryonic notch was found at elevations of approximately the highest modern tidal range (~1 m) and have 'overprinted' the mid-Holocene sea cliff (Figure 6b). This may indicate that the proto-notch starts at the highest tidal range and is developing up/down with slow terrace uplift. The geomorphological characteristics of these notches, i.e., cut at modern high-tide into the vertical Holocene cliff of carbonate bedrock with a symmetric flattened U-shape, may be the result of quiescent conditions during the early stages of notch development. Such overlapping of the former and new erosional zones in Kamaran

458 Island (Figure 6b) corroborates the site's tectonic stability as the former erosional
459 surface does not exceed the modern tidal range. It also suggests that the Kamaran
460 Island has been stable for a considerable time (i.e., for at least the late Pleistocene).
461 Another notch at ~ +4 ± 1 m apmsl (Figure 8b) is thought to be of LIg age, although
462 corals sampled from this terrace were diagenetically altered and yield older ages
463 than the LIg (Table 1).
464
465 A quantitative relationship between notch size, wave energy, and lithology has been
466 suggested (e.g., Antonioli et al., 2015). These authors show that the vertical distance
467 between the roof and the base of the notch is greater than the mean tidal range, but
468 smaller than the maximum difference between tidal extremes (i.e., the maximum
469 and minimum tides). However, this relationship may not be maintained for all
470 notches, and it is not uncommon for notches to have height greater than the tidal
471 range, and up to 3.2 times the tidal range in sheltered/exposed sites (Antonioli et al.,
472 2015). Nonetheless, several studies have linked the width of wave-cut notches (i.e.,
473 the vertical distance between the base and the roof) to the amplitude of the mean
474 tidal range (Trenhaile et al., 1998; Antonioli et al., 2015; Trenhaile, 2015; Rovere et
475 al., 2016; Lorscheid et al., 2017). For example, where the height of the notch is
476 greater than the modern tidal range and assuming the notch was formed by similar
477 processes to today, the difference in the modern and palaeo notch amplitudes can
478 be related to changes in tidal range (e.g., Antonioli et al., 2015; Lorscheid et al.,
479 2017). Such comparisons provide a first-order estimate of possible changes in tidal
480 amplitudes.
481
482 The notches in eastern Kamaran have U-shape morphologies (i.e., notch height
483 exceeds the notch depth), which is greater than the modern tidal range of the area
484 (~1 m). When coupled with the U-notch morphology with the staircase morphology
485 from the same sites (Figure 7), this suggest co-seismic activity, as these terraces lie
486 within the As-Salif Diapir zone. However, sea-level oscillations and/or a sequence of
487 sea-level stillstands related to differences in the tidal regime cannot be excluded.
488 Alternatively, the U-shaped morphologies could suggest that the LIg notches (+3 to
489 +4 m apmsl) were deeper originally, but weak host rocks and prolonged weathering

led to shape modification and roof collapse. The presence of failed cliff material deposited at the toe of Kamaran Island sea cliffs (Figures 6 to 8) would support this interpretation. Deeper notches would require a prolonged contact and/or weak host rocks. Coseismic activity related to the As-Salif salt diapirism to the east of Kamaran Island could also have led to notch displacements and collapse.

5.3 Mid-Holocene sea-level highstand(s)

The global record of mid-Holocene sea level is complex and geographically divergent due to glacio-hydro-isostatic and water redistribution processes (e.g., ocean syphoning at the end of the dominant melting period ~6 to 7 ka) (Clark et al., 1978; Pirazzoli and Pluet, 1991; Mitrovica and Peltier 1991; Mitrovica and Milne, 2002; Lambeck et al., 2014). A sharp decrease in the rate of sea-level rise is predicted after ~6.8 ka, with low rates of change (> 1.42 mm/yr) for the remainder of the Holocene (Antonioli et al., 2015 and references therein). The combined deformation and gravitational response resulted in divergence in the timing and amplitude of the mid-Holocene highstand globally (Nakada and Lambeck, 1987; Pirazzoli and Pluet, 1991; Long, 2001; Mitrovica and Milne, 2002; Milne et al., 2009; Stattegger et al., 2013; Woodroffe and Webster, 2014; Lambeck et al., 2014). A spatially complex pattern is also predicted from the Red Sea, where the isostatic response is largely determined by water-loading (Red Sea, Indian Ocean and Mediterranean) (Lambeck et al., 2011).

Mid-Holocene highstands have been reported for several locations within the Red Sea. The complex spatial variability is expected due to the hydro-isostatic response in the basin to time-dependent water loading (Lambeck et al., 2011). GIA predictions for the Red Sea (e.g. Lambeck et al., 2011; Lambeck et al., 2012) produce high sea levels when ice melt was at its maximum rate, and the highstand is predicted to be more pronounced for both ends of the Red Sea regions compared to the central basin due to water loading from the Indian Ocean and the Mediterranean (Lambeck et al., 2011). In addition, as the glacio-isostatic signal is of the opposite sign to sea-level rise due to melt, mid-Holocene sea-level highstands are not expected for all locations in the Red Sea (Lambeck et al., 2011). Our well-constrained sea-level

521 indicators, and a compilation of previously reported mid-Holocene highstand data
522 (Friedman, 1968, Faure, 1975; Hötzl et al., 1984; Dabbagh et al., 1984; Al-Rifaiy and
523 Cherif, 1988; Gvirtzman et al., 1992; Gvirtzman, 1994; Dullo and Montaggioni, 1998;
524 Plaziat et al., 1995, 1998; El-Asmar, 1997; Carbonne et al., 1998; Moustafa et al.,
525 2000; Shaked et al., 2004) (Figure 11), provide a valuable test of GIA models, Earth
526 model parameter choices for this region, and sea-level predictions given that sea-
527 level amplitudes are strongly Earth model dependent (~1 m at our study sites), with
528 strongest dependence on the upper mantle viscosity (Lambeck et al., 2011). The data
529 from the Yemeni Red Sea are especially useful as to date, observational data is
530 scarce for the southern Red Sea.
531
532 U-series ages of coral samples from two locations on the As-Salif Peninsula (RH and
533 OG) indicate that the terraces and associated geomorphological features are mid-
534 Holocene in age, whereas the corals dated from the ~4 m terrace on Kamaran Island
535 where highly altered and are assumed to be of Last Interglacial in age (Table 1). Our
536 sites on the As-Salif Peninsula suggest some diapir influence, but that this diminishes
537 away from the locus of the diapir, with successively less influence on the elevations
538 of the Om Gedi and Ras Harafa terraces respectively. The two in growth position
539 corals (+0.5 ± 0.2 m apmsl) from the Ras Harafa terrace have mid-Holocene ages
540 (5,358 ± 33 years BP, inverse weighted mean), and are likely a maximum estimate of
541 the age of the mid-Holocene highstand in this region of the southern Red Sea, given
542 that they are below the maximum elevation of the notch cut into the same terrace.
543 The notch itself likely represents the upper limit (elevation +1± 0.2 m apmsl, Figure
544 4) of the mid-Holocene sea-level highstand (i.e., mean sea level) at this site.
545
546 Our new data are broadly consistent with other mid-Holocene sea-level data for the
547 Red Sea (Figure 11), and show the drop in relative sea level after the cessation of the
548 main melt period at ~6 ka (Nakada and Lambeck, 1987; Mitrovica and Milne, 2002;
549 Antonioli et al., 2015; Lambeck et al., 2014). In general, the more northerly sites
550 have higher elevation mid-Holocene terraces, and older ages for the terraces than
551 for the sites in Saudi Arabia at the centre of the basin (Figures 11 and 12) (Friedman,

552 1968; Gvirtzman, et al., 1992; Gvirtzman, et al., 1994; El-Asmer, 1997; Dullo and
553 Montaggioni, 1998; Plaziat et al., 1998; Moustafa et al., 2000; Shaked et al., 2002;
554 Faur, 1975; Hötzl et al., 1984; Hein et al., 2011), which is in broad agreement with
555 GIA predictions for the mid-Holocene (Lambeck et al., 2011). Our new Yemen data
556 also show older ages for the southern edges of the basin, and the elevation of the
557 highstand is close to that predicted (~0.5 m) using the preferred Earth model (E3) of
558 Lambeck et al. (2011). In detail, the elevation of our Yemen samples is very similar
559 to the elevations given for the fossil terraces of Saudi Arabia (Dullo and Montaggioni,
560 1998), where a "lower" highstand is predicted, and also similar in elevation to
561 portions of the Egyptian coast (24 to 26 °N; Plaziat et al., 1995, 1998), where a
562 "higher" highstand are predicted from GIA modelling (cf. Lambeck et al., 2011).
563 There may be tectonic, or neotectonic (e.g., due to salt diapirism) overprinting of the
564 elevations and sea-level signal at other sites, but which have been explicitly
565 accounted for in our study using local and regional mapping. This allowed us to
566 disentangle the neotectonic overprinting and to determine the most likely elevation
567 for the mid-Holocene highstand at the Ras Harafa site (i.e., the elevation of the
568 notch at elevation +1± 0.2 m apmsl, Figure 4). Further data from the Red Sea, and
569 the southern Red Sea in particular, is needed to more fully test the GIA models and
570 associated sea-level predictions. A sufficiently dense geographical coverage is still
571 lacking, and factors other than sea level (e.g., neotectonics) need to be disentangled
572 by careful mapping at local/regional scales.
573
574 In summary, our observations from the southern Red Sea, compare favorably with
575 the GIA prediction models of Lambeck et al. (2011), where the highest and earliest
576 mid-Holocene sea levels occur between 6 to 5 ka in the southern (and northern) Red
577 Sea basin and also with other observational data (Friedman, 1968, Faur, 1975; Hötzl
578 et al., 1984; Gvirtzman et al., 1992; Gvirtzman, 1994; Dullo and Montaggioni, 1998;
579 Moustafa et al., 2000; Shaked et al., 2002; Hein et al., 2011) from the basin (Figure
580 12). However, more high-quality data, with well constrained age and elevation
581 uncertainties, is required to more fully test both the GIA predictions and Earth model
582 parameter choices for the region.
583

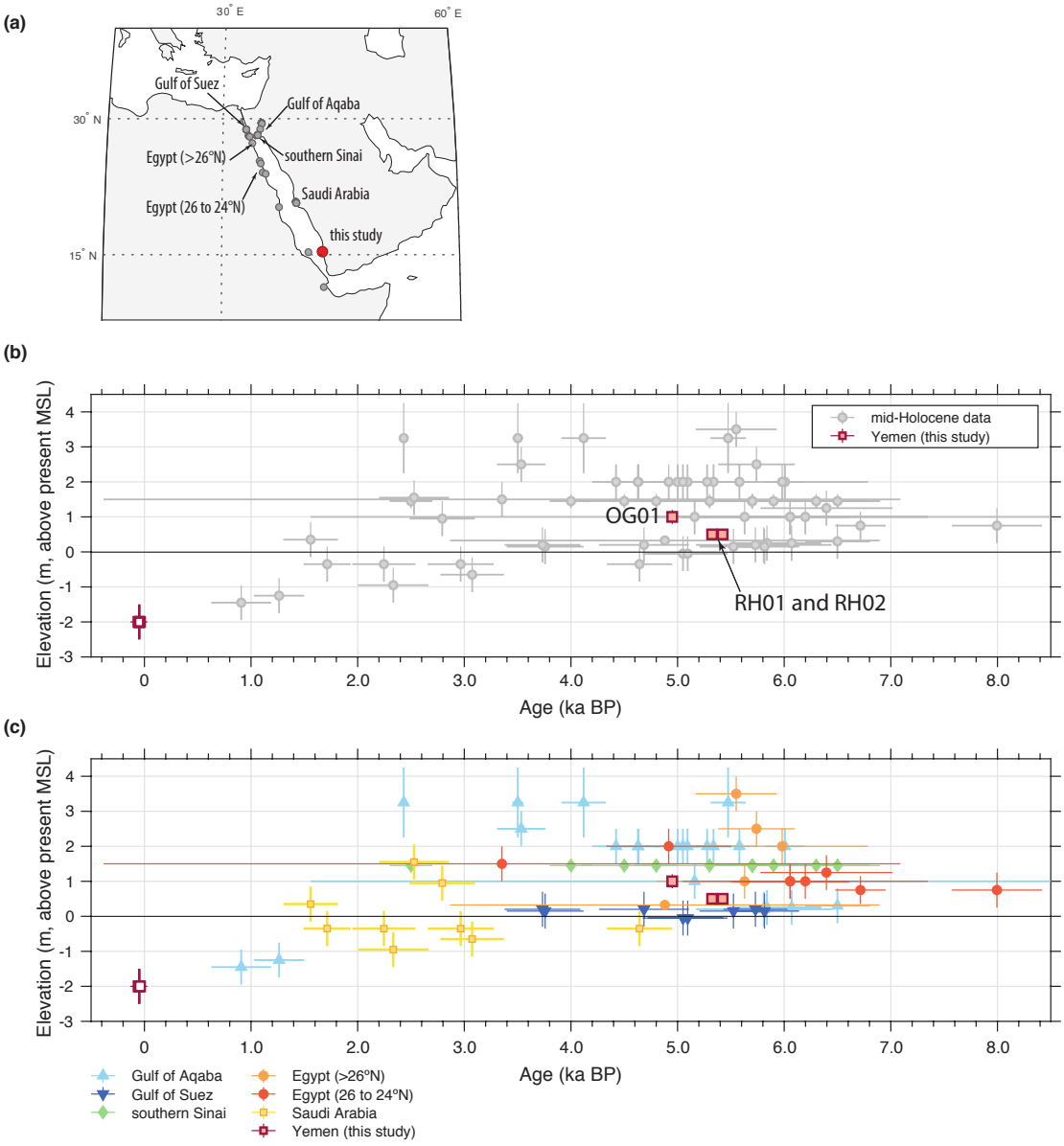

Figure 11: Elevation of the mid-Holocene highstand in the Red Sea. (a) map of mid-Holocene highstand sites (b) grey dots, reported mid-Holocene elevations and ages (Friedman, 1968, Faur, 1975, Hötzl et al., 1984; Gvirtzman, 1994; Gvirtzman et al., 1992; Dullo and Montaggioni, 1995, 1998; Al-Raifaiy and Cherif, 1988; Moustafa et12 al., 2000; Shaked et al., 2002; Hein et al., 2011) (radiocarbon ages have been recalibrated using the latest calibration curve (Marine20, Heaton et al., 2020) and a consistent ΔR (weighted mean ΔR = 176 ± 62 years (n = 9), Cember, 1989; Felis et al., 2004; Reimer and Reimer, 2020); filled red squares, dated fossil from As-Salif Peninsula and, open red squares, dated modern coral samples from Bab El-Mandab; (c) as in (b) but separated geographically by latitude. Uncertainties in age and

595 elevation are 2 sigma. (The compiled data is available here: doi:

596 10.6084/m9.figshare.13079240)

597

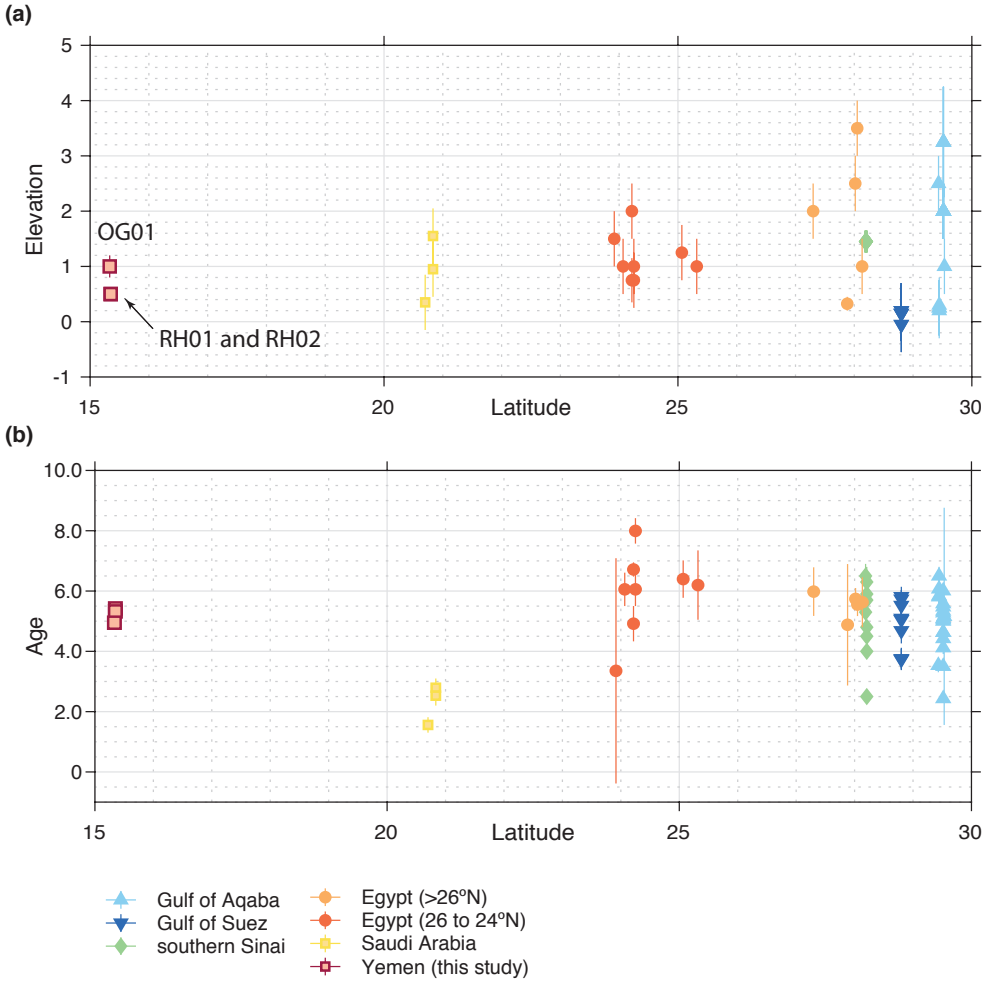

Figure 12: Elevation of the mid-Holocene highstand in the Red Sea. (a) grey dots, reported mid-Holocene elevations and ages (Friedman, 1968; Faur, 1975; Hötzl et al., 1984; Gvirtzman et al., 1992; Gvirtzman, 1994; Dullo and Montaggioni, 1995, 1998; El-Asmar, 1997; Moustafa et al., 2000; Shaked et al., 2002; Hein et al., 2011) (radiocarbon ages have been recalibrated using the latest calibration curve (Marine20, Heaton et al., 2020) and a consistent ΔR (weighted mean ΔR = 176 ± 62 years (n = 9), Cember, 1989; Felis et al., 2004; Reimer and Reimer, 2020); red squares, elevations of dated coral samples, this study; (b) as in (a) but separated geographically by latitude. Uncertainties in age and elevation are 2 sigma. (The compiled data is available here: doi: 10.6084/m9.figshare.13079240).

598 **5.4 Tectonic Stability, neotectonics and salt diaprism in the Yemeni Red Sea**

599 The development of the southern Red Sea islands and volcanic coastal formations
600 has been primarily controlled by tectonics since the opening of the rift (Purser and
601 Hötzl, 1988; Bosworth, 1994, 2015; Bosence, 2005; Rowlands and Purkis, 2015). Our
602 study area (Kamaran and As-Salif Peninsula) is part of a salt diapir platform formed
603 by a linear north-south trending salt diapir, which is bounded by a normal growth
604 fault on the eastern margin and continues offshore for several kilometers (Bosence
605 et al., 1998). The orientation of the island terraces in the southern Red Sea are
606 closely related to fault lineaments, and the fault trends are also allied with swarm of
607 high magnitudes earthquakes along the offshore of Kamaran and As-Salif regions.
608
609 The Yemeni Red Sea generally has lower seismicity and uplift compared to the
610 northern part of the Red Sea and tectonic movements here are more localized and
611 associated with salt diapirism. Seismic activity and tensional movements in the
612 study region have stimulated the evaporites to rise and form a salt dome ~+18 m
613 apmsl. The underlying evaporite unit makes the sites are more susceptible to
614 localized crustal movements due to salt tectonics (Bosence et al., 1998). However,
615 the influence of salt diapirism and/or tectonics appears limited and highly localized
616 in the area, given the similarity in the elevation of the mid-Holocene notches on the
617 As-Salif Peninsula (RH and OG), and Kamaran Island (+0.5 ± 0.2 m apmsl). However,
618 we detect some limited neotectonism at the eastern Karaman Island site, where the
619 terrace is uplifted up to ~ + 6 ±1 m (apmsl) relative to the main island, which has an
620 elevation of ~ + 4 ±1 m (apmsl) (Figure 6a). The contrast in the faults flank elevations
621 was a result of movement of the hanging-wall (seaward side) up relative to the
622 stable footwall (landward side), suggests a thrust (reversed) fault. The fault can be
623 easily traced as a discrepancy between the mid-Holocene wave cut cliff (at ~ +1.3 ±
624 0.2 m elevation) and the well-developed U-shape mid-Holocene wave-cut notch of ~
625 + 2.3 ± 0.2 m elevation. As the displaced layer is imprinted with an embryonic notch
626 at the same height as the sea, the age of this fault is not older than the mid-
627 Holocene, and is probably linked with the complex activity of the salt diaper.
628
629 Northern Kamran Island is sufficiently far from the influence of the salt diapir that

630 the notches retain their asymmetrical V-shape. This is in contrast to the eastern
631 portion of the island where coseismic activity associated with salt diapirism has likely
632 contributed to modified the morphology of wave-cut cliffs and notches resulting in
633 U-shaped notches. The change in the erosional base (which is limited by the tidal
634 range) may also have been prompted by changes in sea level, wave energy and/or
635 tidal regime leading to a widening, deepening and separation of notches and
636 possible overprinting of older features (Schneiderwind et al., 2017).
637
638 **6. CONCLUSIONS**
639 We document palaeo sea-level indicators (fossil terraces, wave-cut notches and sea
640 cliffs) for two locations (As-Salif and Karaman Island) in the Yemeni southern Red Sea
641 and, using U-series dates of fossil corals in the same (underlying) unit, quantify the
642 changes in sea level during the mid-Holocene and LIg. The spatial distribution,
643 morphology and elevations of fossil terraces allowed us to disentangle the various
644 processes, including the history of recent tectonic uplift. The relative consistency of
645 the mid-Holocene geomorphic features suggests relative tectonic stability of the
646 region with some minor diapir influence. These new observations improve our
647 understanding of the local and regional history, providing constraints on the long-
648 term rates of vertical movement that underpin models of Red Sea rifting.
649 Additionally, given the relatively stable tectonic setting for the last ~6,000 years, the
650 study locations, should be useful for reconstructing past sea-level changes.
651
652 We demonstrate the potential of tidal notches for reconstructing past changes in sea
653 level in the region. Despite complications in the field (i.e., the obstruction of the
654 vertex due to cliff failure), our new observations and detailed mapping of
655 geomorphic features enabled us to account for neotectonics (e.g., salt diapirism,
656 localised faulting). This allowed us to establish the elevation of the mid-Holocene
657 highstand from wave-cut notches at ~1 ± 0.2 m (apmsl).
658
659 Our new southern Red Sea data thereby provide a valuable calibration dataset for
660 geophysical models of the region, particularly as data for the southern Red Sea basin
661 was previously lacking. Our new data, and compilation of the wider regional mid-

Holocene data suggest that the preferred Earth model parameters of Lambeck et al. (2011) provide sea-level predictions that are consistent with the available evidence. Our data go some way to addressing the 'incomplete record' of Holocene sea-level change in the Red Sea identified by Lambeck et al. (2011). However, more high-quality data is required.

The Yemeni Red Sea generally has lower seismicity and uplift compared to the northern part of the Red Sea, and tectonic movements here are more localized and associated with salt diapirism. However, some limited neotectonism in the eastern portion of the island has likely contributed to modify the morphology of wave-cut cliffs and notches resulting in U-shaped notches.

Acknowledgements

This project was funded by U.S Fulbright program and is a research scholarship given to the first author. The help extended by Prof. Mohammed Al-Wosabi and Dr. Aref Al-Sageer during the fieldwork is gratefully acknowledged. Many thanks go to Julie Retrum, Mellissa Cross, Yanbin for their help during U-isotope analysis at the University of Minnesota. Special thanks go to Rick Knurr for assistance in XRD analysis. Einas Al-Alimey, a Cultural Affairs Specialist at the U.S Embassy in Sana'a was of great help to this study. We are most grateful to Christopher Hein (Virginia Institute of Marine Science) for detailed reviews and comments that led to substantial improvements to this work.

References

Al-Mikhlafi, A.S., Edwards, R.L., Cheng, H., 2018. Sea-level history and tectonic uplift during the last-interglacial period (LIG) inferred from the Bab al-Mandab coral reef terraces, Yemen, *J. Afr. Earth Sci.*, 138, 133-148.

Al-Nakhal, H. and Alaug, A.S., 2013. Nomenclature review of the rock units in the stratigraphic lexicon of Yemen, Iranian Journal of Earth Sciences, 5: 82-99.

Al-Rifaiy, I., Cherif, O., 1988. The fossil coral reefs of A1 Aqaba, Jordan. *Facies* 18: 219 - 230. doi:10.1007/BF02536801.

694 Andersen, M.B., Stirling, C.H., Potter, E.K., Halliday, A.N., Blake, S.G., McCulloch,
695 M.T., Ayling, B.F., O'Leary, M.J., 2010. The timing of sea-level high-stands during
696 Marine Isotope Stages 7.5 and 9: constraints from the uranium-series dating of
697 fossil corals from Henderson Island. Geochim. Cosmochim. Acta 74, 3598–3620.
698 Angelucci, A., Boni, C.F., Bono, P. et al., 1985. L'archipelago delle Isole Dahlak ncl Mar
699 Rosso meridionale: alcune caratteristiche geologiche. *Bollettino della Societa*
700 *Geografica Italiana*, Ser. XI, Vol. II, 233- 262.
701 Angelucci, A., Matteucci, R ., Praturlon, A., 1981. Outline of geology and sedimentary
702 environments of the Dahlak Islands (southern Red Sea): *Bollettino della Societa*
703 *Geografica Italiana*, v. 99, pp. 405-419, Roma.
704 Antonioli, F., Anzidei, M., Amorosi, A., Lo Presti, V., Mastronuzzi, G., Deiana, G., De
705 Falco, G., Fontana, A., Fontolan, G., Lisco, S., Marsico, A., Moretti, M., Orrù,
706 P.E., Sannino, G.M., Serpelloni, E., Vecchio, A., 2017. Sea-level rise and
707 potential drowning of the Italian coastal plains: flooding risk scenarios for
708 2100. Quat. Sci. Rev. 158, 29-43.
709 https://doi.org/10.1016/j.quascirev.2016.12.021.
710 Antonioli, F., Ferranti, L., Lambeck, K., Kershaw, S., Verrubbi, V., Dai Pra, G., 2006.
711 Late Pleistocene to Holocene record of changing uplift rates in southern
712 Calabria and northeastern Sicily (southern Italy, Central Mediterranean Sea).
713 Tectonophysics 422, 23-40.
714 Antonioli, F., Lo Presti, V., Rovere, A., Ferranti, L., Anzidei, M., Furlani, S.,
715 Mastronuzzi, G., Orru, P.E., Scicchitano, G., Sannino, G., Spampinato, C.R.,
716 Pagliarulo, R., Deiana, G., de Sabata, E., Sanso, P., Vacchi, M., Vecchio, A.,
717 2015. Tidal notches in Mediterranean Sea: a comprehensive analysis. Quat.
718 Sci. Rev. 119, 66-84. https://doi.org/10.1016/j.quascirev.2015.03.016.
719 Bard, E., Fairbanks, R.G., Hamelin, B., Zindler, A., Hoang, C.T., 1991. Uranium-234
720 anomalies in corals older than 150,000 years. Geochim. Cosmochim. Acta 55,
721 2385 - 2390.
722 Beydoun, Z.R., As-Saruri, M.L., El-Nakhal, H., Al-Ganad, I.N., Baraba, R.S., Nani, A.O.,
723 Al-Aawah, M.H., 1998. International lexicon of stratigraphy, Republic of Yemen.
724 VIII, Asia, fasc, 10b2. 34. IUGS Publ., pp. 1–245.
725 Bird, E.C.F., 2000. Coastal geomorphology: an introduction. Wiley, Chichester, p 322

Bosence, D. w. J.; Al-Aawah, M. H.; Davison, I.; Rosen, B. R.; Vita-Finzi C.; Whitaker, E., 1998. Salt domes and their control on basin margin sedimentation: a case study from the Tihama Plain, Yemen, in *Sedimentation and Tectonics of Rift Basins: Red Sea-Gulf of Aden* (eds B.H. Purser and D.W.J. Bosence), Chapman & Hall, London, pp. 448-464.

Bosence, D., 2005. A genetic classification of carbonate platforms based on their basinal and tectonic settings in the Cenozoic. Sediment Geol. 175, 49-72.

Bosworth W., 2015. Geological evolution of the Red Sea: Historical background, review, and synthesis. In: Rasul NMA, Stewart ICF (eds) The Red Sea. Springer Earth System Sciences, Springer-Verlag Berlin Heidelberg, pp 45-78. https://doi.org/10.1007/978-3-662-45201-1_1.

Bosworth, W., 1994. A model for the three-dimensional evolution of continental rift basins, north-east Africa. In: Schandelmeier, H., Stern, R.J. (Eds.), Geology of Northeast Africa (Part 2), Geologische Rundschau 83, pp. 671–688.

Brown, G.F., 1970. Eastern margin of the Red Sea and the coastal structures in Saudi Arabia. Philos Trans R Soc Lond Ser A, Math Phys Sci 267:75–87

Carbonne, F.; Matteucci, R.; Angelucci, A., 1998. Present-day sedimentation of the carbonate platforms of the Dahlak Islands, Eritrea, in Sedimentation and tectonics of rift basins: Red Sea-Gulf of Aden, (eds B.H. Purser and D.WJ. Bosence), Chapman & Hall, London, pp. 527-542.

Carobene, L., 2015. Marine notches and sea-cave bioerosional grooves in microtidal areas : examples from the Tyrrhenian and Ligurian coasts-Italy. J. *Coast Res*. 31, 536-556. https://doi.org/10.2112/JCOASTRES-D-14-00068.1.

Cember, R P, 1989. Bomb Radiocarbon in the Red Sea: A medium-scale gas exchange experiment. J. Geophys. Res. 94(C2), 2111-2123.

Chen, J.H., Curran, H.A., White, B., Wasserburg, G.J., 1991. Precise chronology of the last interglacial period: ^{234}U-^{230}Th data from fossil coral reefs in the Bahamas. Geol. Soc. Am. Bull. 103, 82-97.

Cheng, H., Edwards, R.L., Shen, C-C., Woodhead, J., Hellstrom, J., Wang, Y.J., Kong, X.G., Spötl, C., Wang, X.F., Alexander, Jr, E.C., 2013. Improvements in ^{230}Th dating, ^{230}Th and ^{234}U half-life values, and U-Th isotopic measurements by

multi-collector inductively coupled plasma mass spectrometry. Earth and Planet. Sci. Lett., 371–372, 82–91.

Cheng, H., Edwards, R.L., Wang, X.F., Woodhead, J., Hellstrom, J., Wang, Y.J., Kong, X.G., 2008. A new generation of ^{230}Th dating techniques: tests of precision and accuracy. Geochim. Cosmochim. Acta. 72, 12S.

Clark, J.A., Farrell, W.E., Peltier, W.R., 1978. Global changes in post glacial sea-level: a numerical equation. Quat. Res. 9, 265-287.

Clifford, M., Horton, C., Schmitz, J., Kantha, L.H., 1997. An oceanographic nowcast/forecast system for the Red Sea. J. Geophys. Res. Ocean. 102, 25101-25122.

Connolly, J.R., 2010. Introduction to x-Ray power diffraction, Springer 2010. http://www.ccp14.ac.uk/index.html.

Dabbagh, A.; Hötzl, H., Schnnier, H., 1984. Farasan Islands, In Jado AR, Zoetl JG (eds). Quaternary period in Saudi Arabia, Volume 2: Springer-Verlag, Vienna, Austria, pp. 212–220.

Davison, I., Al-Kadasi, M., Al-Khirbash, S., Al-Subbary, A., Baker, J., Blakey, S., Bosence, D., Dart, C., Heaton, R., Heaton, R., McClay, K., Menzies, M., Nichols, G., Owen, L., Yelland, A., 1994. Geological evolution of the southeastern Red Sea Rift margin, Republic of Yemen, Geol. Soc. Am Bull. 106, 1474-1493.

Davison, I., Bosence, D., Alsop, I., Al-Aawah, M.H., 1996. Deformation and sedimentation around active Miocene salt diapirs on the Tihama Plain, northwest Yemen, in Salt Tectonics (eds I. Alsop, D. Blundell and I. Davison), Geol. Soc. Spec. Publ. 100, pp. 23-39.

Defant A (1961) Physical oceanography. Pergamon Press, 598 pp

Dullo WC, Montaggioni L., 1998. Modern Red Sea coral reefs: a review of their morphologies and zonation. In: Purser BH, Bosence DWJ (eds) Sedimentation and tectonics of rift basins: Red Sea-Gulf of Aden. Chapman and Hall, London, pp 583-594. https://doi.org/10.1007/978-94-011-4930-3_31

Edelman-Furstenberg, Y., Scherbacher, M., Hemleben, C. and Almogi-Labin, A., 2001. Deep-sea benthic foraminifera from the central Red Sea. J Foramin Res 31, 48 - 59.

788 Edwards, F. J. 1987. Climate and oceanography. *In:* EDWARDS, F. J. & HEAD, S. M.
789 (eds) *Red Sea – Key Environments.* Pergamon Press, Oxford, 45-69.
790 Edwards, R.L., Chen, J.H., Ku, T.-L., Wasserburg, G.J., 1987. Precise timing of the last
791 interglacial period from mass spectrometric analysis of 230Th in corals. Science
792 236, 1547-1553.
793 El-Asmar, H.M., 1997. Quaternary isotope stratigraphy and paleoclimate of coral reef
794 terraces, Gulf of Aqaba, south Sinai, Egypt. Quat. Sci. Rev. 16, 911-924.
795 El-Nakhal, H., Alaug, A.S., 2013. Nomenclature review of the rock units in the
796 stratigraphic Lexicon of Yemen. Iranian Journal of Earth Science 5, 82-99.
797 Evelpidou, N., Vassilopoulos, A., Pirazzoli, P.A., 2012. Submerged notches on the
798 coast of Skyros Island (Greece) as evidence for Holocene subsidence.
799 Geomorphology, 141-142, 81-87.
800 Faivre, S., Bakran-Petricioli, T., Horvatincic, N., Sironic, A., 2013. Distinct phases of
801 relative sea-level changes in the central Adriatic during the last 1500 years-
802 influence of climatic variations? Palaeo. Palaeo. Palaeo. 369, 163 -174.
803 Faure, H., 1975. Recent crustal movements along the Red Sea and Gulf of Aden in
804 Afar (Ethiopia and T.F.A.I). Tectonophysics 29, 479-486.
805 Felis, T., Lohmann, G., Kuhnert, H., Lorenz, S.J., Scholz, D., Patzold, J., Al-Rousan, S.A.,
806 and Al-Moghrabi, S.M., 2004. Increased seasonality in Middle East
807 temperatures during the last interglacial period. Nature 429, 164-168.
808 Friedman, G. M., 1968. Geology and geochemistry of reefs, carbonate sediments,
809 and waters, Gulf of Aqaba (Elat), Red Sea. *J. Sediment.Petrol.*, 38, 895-919.
810 Florea, L.J., Vacher, H.L., Donahue, B., Naar, D., 2007. Quaternary cave levels in
811 peninsular Florida. Quat. Sci. Rev. 26, 1344-1361.
812 Friedman, G.M., 1968. Geology and geochemistry of reefs, carbonate sediments, and
813 waters, Gulf of Aqaba (Elat), Red Sea. J. Sediment. Petrol. 38, 895-919.
814 Gallup, C.D., Edwards, R.L., Johnson, R.G., 1994. The timing of high sea levels over
815 the past 200,000 years. Science 263, 796-800.
816 Girdler, R.W., Styles, P., 1974. Two stage Red Sea floor spreading. Nature 247, 7-11.
817 Gracia, F.J., Rodriguez-Vidal, Caceres, L.M., Belluomini. G., Benavente, J., Alonso, C.,
818 2008. Diapiric uplift of an MIS 3 marine deposit in SW Spain: Implications for

819 Late Pleistocene sea level reconstruction and palaeogeography of the Strait of
820 Gibraltar. Quat. Sci. Rev. 27, 2219-2231.
821 Gvirtzman, G., 1994. Fluctuations of sea level during the past 400,000 years: The
822 record of Sinai, Egypt (northern Red Sea). Coral Reefs 13, 203–214.
823 doi:10.1007/BF00303633.
824 Gvirtzman, G., Kronfeld, J., Buchbinder, B., 1992. Dated coral reefs of southern Sinai
825 (Red Sea) and their implication to late Quaternary sea levels. Mar. Geol. 108,
826 29-37.
827 Gvirtzman, G., Friedman, G.M., Miller, D.S., 1973. Control and distribution of
828 uranium in coral reefs durng diagenesis. J Sedim Petrol 43, 985-997.
829 Hamelin, B., Bard, E., Zindler, A., Fairbanks, R.G., 1991. $^{234}U/^{238}U$ mass spectrometry
830 of corals: how accurate is the U-Th age of the last interglacial period? Earth
831 Planet. Sci. Lett. 106, 169–180.
832 Hearty, P.J., Hollin, J.T., Neumann, A.C., O'leary, M.J., McCulloch, M., O'Leary, M.J.,
833 2007. Global sea-level fluctuations during the Last Interglaciation (MIS 5e). Quat.
834 Sci. Rev. 26, 2090-2112. https://doi.org/10.1016/j.quascirev.2007.06.019.
835 Heaton, R.C., Jackson, M.P.A., Bamahmoud, M. and Nani, A.S.O., 1996. Superposed
836 Neogene extension, contraction, and salt canopy emplacement in the Yemeni
837 Red Sea, in Salt Tectonics; A Global Perspective for Exploration (eds M.P.A.
838 Jackson, D.G. Roberts and S. Snelson). Am. Assoc. Petr. Geol. Mem. 65, pp. 333-
839 351.
840 Heaton, T. J., Köhler, P., Butzin, M., Bard, E., Reimer, R. W., Austin, W. E. N., Bronk
841 Ramsey, C., Grootes, P. M., Hughen, K. A., Kromer, B., Reimer, P. J., Adkins, J.,
842 Burke, A., Cook, M. S., Olsen, J. and Skinner, L. C. 2020. Marine20—The Marine
843 Radiocarbon Age Calibration Curve (0–55,000 cal BP), Radiocarbon 62(4), 779–
844 820. doi: 10.1017/RDC.2020.68
845 Hein, C.J., FitzGerald, D.M., Milne, G.A., Bard, K., Fattovich, R., 2011. Evolution of a
846 Pharaonic harbor on the Red Sea: Implication for coastal response to changes in
847 sea level and climate, Geology 39, 687-690. doi: 10.1130/G31928.1
848 Hempton, M.R., 1987. Constraints on Arabian plate motion and extensional history
849 of the Red Sea. Tectonics 6, 687-705.
850 Hibbert, F.D., Rohling, E.J., Dutton, A., Williams, F.H., Chutcharavan, P.M., Zhao, C.,

Tamisiea, M.E., 2016. Coral indicators of past sea-level change: a global repository of U-series dated benchmarks. Quat. Sci. Rev. 145, 1-56. https://doi.org/10.1016/j.quascirev.2016.04.019.

Hötzl, J.G., 1984. The Red Sea. In: Jado, A.R., Hötzl, J.G. (Eds.), Quaternary Period in Saudi Arabia, vol. 2. Springer, Vienna, pp. 13-25.

Hötzl, 1984, H., Jado, A.R., Moser, H., Rauert, W. and Zotl, J.G., 1984. The youngest Pleistocene, In: Jado, A.R., Hötzl, J.G. (Eds.), Quaternary Period in Saudi Arabia, vol. 2., Springer, Vienna, pp. 314-324.

Jaffey, A.H., Flynn, K.F., Glendenin, L.E., Bentley, W.C., Essling, A.M., 1971. Precision measurement of half-lives and specific activities of ^{235}U and ^{238}U. *Phys. Rev. C* 4, 1889 -1906.

Kelletat, D., Scheffers, A., 2005. Ergänzende Informationen zum Sumatra-Andaman-Tsunami vom 26.12.2004. Geographische Rundschau 57 (9): 64-65.

Kelsey, H.M., 1990. Late Quaternary deformation of marine terraces on the Cascadia subduction zone near Cape Blanco, Oregon. Tectonics 9, 983–1014.

Kelsey, H.M., and Bockheim, J.G., 1994. Coastal landscape evolution as a function of eustasy and surface uplift rate, Cascadia margin, southern Oregon. Geol. Soc. Am. Bull. 106, 840–854.

Kershaw, S., Guo, L., 2001. Marine notches in coastal cliffs: indicators of relative sea-level chnge, Perachors Peninsula, central Greece, Marine Geology 179, 213-228.

Lambeck, K., Purcell, A., Dutton, A., 2012. The anatomy of interglacial sea-levels: The relationship between sea-levels and ice volumes during the Last Interglacial. Earth Planet. Sci. Lett. 4-11, 351-316. doi:10.1016/j.epsl.2011.08.026.

Lambeck, K., Purcell, A., Flemming, N.C., Vita-Finzi, C., Alsharekh, A.M., Bailey, G.N., 2011. Sea level and shoreline reconstructions for the Red Sea: isostatic and tectonic considerations and implications for hominin migration out of Africa. Quat. Sci. Rev. 30, 3542-3574. http://dx.doi.org/10.1016/j.quascirev.2011.08.008.

Lambeck, K., Rouby, H., Purcell, A., Sun, Y., Sambridge, M., 2014. Sea level and global ice volumes from the Last Glacial Maximum to the Holocene. Proc. Natl. Acad. Sci. U.S.A. 111(43), 15296-15303, doi:10.1073/pnas.1411762111.

882 Lamy, F., Arz, H.W., Bond, G.C., Bahr, A. and Patzold, J., 2006. Multicentennial-scale
883 hydrological change in the Black Sea and northern Red Sea duing the Holocene
884 and the Arctic/North Atlantic Oscillation, Paleoceanography 21, 1-11.
885 doi:10.1029/2005PA001184
886 Langodan, S., Cavaleri, L. , Pomaro, A., Portilla, J., AbuAlNaja, Y., Hoteit, I., 2018.
887 Unraveling climatic wind and wave trends in the Red Sea using wave spectra
888 partitioning: J. of Climate. 31, 1881-1895. DOI: 10.1175/JCLI-D-17-0295.1
889 Langodan S., Cavaleri, L., Pomaro, A., Viswanadhapalli, Y, Bertotti L. Hoteit, I., 2017.
890 The climatology of the Red Sea-part 2: the waves. Int. J. Climat. DOI:
891 10.1002/joc.5101.
892 Long, A., 2001. Mid-Holocene sea-level change and coastal evolution. *Prog. Phys.*
893 *Geogr*. 25, 399 - 408.
894 Lorscheid, T., Stocchi, P., Casella, E., G_omez-Pujol, L., Vacchi, M., Mann, T., Rovere,
895 A., 2017. Paleo sea-level changes and relative sea-level indicators: precise
896 measurements, indicative meaning and glacial isostatic adjustment perspectives
897 from Mallorca (Western Mediterranean). *Palaeogeogr. Palaeoclimatol.*
898 *Palaeoecol.*473, 94-107. https://doi.org/10.1016/j.palaeo.2017.02.028.
899 May, V.J., Heeps, C., 1985. The Nature and Rates of Change on Chalk
900 coastlines. Zeitschrift für Geomorphologie NF Suppl. Band 57, 81-94.
901 Milne, G.A., Gehrels, W.R., Hughes, C.W., Tamisiea, M.E., 2009. Identifying the
902 causes of sea-level change. *Nat. Geosci*. 2, 471-478.
903 Milne G. A., Mitrovica J. X., 2008. Searching for eustasy in deglacial sea level
904 histories. Quat Sci Rev. 27, 2292-2302. doi:10.1016/j.quascirev.2008.08.018.
905 Mitchell, D.J.W., Allen, R.B., Salama, W., Abduzakm, A., 1992. Tectonostratigraphic
906 framework and hydrocarbon potential of the Red Sea. J Petrol. Geol. 15 (2),
907 187–210
908 Mitrovica, J.X., Milne, G.A., 2002. On the origin of late Holocene sea-level highstands
909 within equatorial ocean basins. Quat. Sci. Rev. 21, 2179-2190.
910 doi:10.1016/S0277-3791(02)00080-X.
911 Mitrovica, J.X., Peltier, W.R., 1991. On postglacial geoid subsidence over the
912 equatorial oceans. J. Geophys. Res. 96 (B12), 20053-20071.
913 Moses, C.A., 2013. Tropical rock coasts: Cliff, notch and Platform erosion dynamics,

914 Progress in Physical Geography 37, 206-226. DOI: 10.1177/0309133312460073
915 Moustafa, Y.A., Patzold, J., Loya, Y., Wefer, G., 2000. Mid-Holocene stable isotope
916 record of corals from the northern Red Sea, International Journal of Earth
917 Sciences 88, 742–751, 2000.
918 Nakada, M., Lambeck, K., 1987. Glacial rebound and relative sea-level variations: a
919 new appraisal. Geoph. J. R. Astron. Soc. 90, 171-224.
920 Neumann, A.C., Hearty, P.J., 1996. Rapid sea-level changes at the close of the last
921 interglacial (substage 5e) recorded in Bahamian island geology. Geology 24, 775-
922 778.
923 Pedoja, K., Husson, L., Johnson, M.E., Melnick, D., Witt, C., Pochat, S. et al., 2014.
924 Coastal staircase sequence reflecting sea-level oscillations and tectonic uplift
925 during the Quaternary and Neogene. Earth-Sci. Rev. 132, 13-38.
926 Phillips, B.A.M., 1970. The significance of inheritance in the interpretation of marine
927 and lacustrine coastal histories. Lakehead University Review 3, 36–45.
928 Pirazzoli, P.A., Evelpidou, N., 2013. Tidal notches: a sea-level indicator of uncertain
929 archival trustworthiness. Palaeogeogr. Palaeoclimatol. Palaeoecol. 369, 377-384.
930 Pirazzoli, P.A., Stiros, S.C., Arnold, M., Laborel, J., Laborel-Deguen, F., Papageorgiou,
931 S., 1994a. Episodic uplift deduced from Holocene shorelines in the Perachora
932 Peninsula, Corinth area, Greece. Tectonophysics 229, 201–209.
933 Pirazzoli, P.A., Stiros, S.C., Laborel, J., Laborel-Deguen, F., Arnold, M., Papageorgiou,
934 S., Morhange, C., 1994b. Late-Holocene shoreline changes related to
935 palaeoseismic events in the Ionian Islands, Greece. *The Holocene* 4, 397–405.
936 Pirazzoli, P.A., Pluet, J., 1991. World atlas of Holocene sea-level changes. Elsevier
937 Oceanogr. Ser. 58, 299
938 Pirazzoli, P.A., 1986. Marine notches. In: van de Plassche, O. (Ed.), Sea-level
939 Research: a Manual for the Collection and Evaluation of Data. Geo Books,
940 Norwich, pp. 361-400.
941 Plaziat, J.-C., Baltzer, F., Chouki, A., Conchon, O., Freytet, P., Orszag-Sperber, F.,
942 Raguideau, A., Reyss, J.-L., 1998. Quaternary marine and continental
943 sedimentation in the northern Red Sea and Gulf of Suez (Egyptian coast):
944 influences of rift tectonics, climatic changes and sea-level fluctuations. In:
945 Purser, B.H., Bosence, D.W.J. (Eds.), Sedimentation and Tectonics in Rift Basins:

946 Red Sea—Gulf of Aden. Chapman and Hall, London, pp. 537–573.
947 Plaziat J.-C., Baltzer F., Choukri A., Conchon O., Freytet P., Orszag-Sperber F., Purser
948 B.H., Raguideau A., Reyss J.-L., 1995. Quaternary changes in the Egyptian shore-
949 line of the northwestern Red Sea and Gulf of Suez. Quaternary International,
950 Amsterdam 29-30, 11-22.
951 Purkis S.J., Harris P.M., Ellis J., 2012. Patterns of sedimentation in the contemporary
952 Red Sea as an analog for ancient carbonates in rift settings. J. Sediment. Res. 82,
953 859-870.
954 Purkis, S.J., Riegl, B.M., 2012. Geomorphology and reef building in the SE Gulf. In:
955 Coral reefs of the Gulf: adaptation to climatic extremes hardcover. Springer,
956 Netherlands. ISBN 978-94-007-3007-6
957 Purser, B.H., Hötzl, H., 1988. The sedimentary evolution of the Red Sea rift: a
958 comparison of the northwest (Egyptian) and northeast (Saudi Arabian) margins.
959 Tectonophysics, 153, 193-208.
960 Ralston, D.K., Jiang, H., Ferrar, T.F., 2013. Waves in Red Sea: Response to monsoonal
961 and mountain gap winds. Cont. Shelf Res. 65, 1–13.
962 *https://doi.org/10.1016/j.csr.2013.05.017*.
963 Reimer, P.J., Reimer, R.W., 2020. Marine reservoir correction database.
964 http://calib.org/marine/ (accessed 12th Oct 2020).
965 Rodriguez-Vidal, J., Caceres, L.M., Abad, M., Ruiz, F., Martinez-Aguirre, A. 2007.
966 Morphosedimentary evidence of the Last Interglacial Maximum on the coast of
967 Governor's Beach, Gibraltar, Geogaceta 42, 107-110.
968 Rovere, A., Hearty, P.J., Austermann, J., Mitrovica, J.X., Gale, J., Moucha, R., Forte,
969 A.M., Raymo, M.E., 2015. Mid-Pliocene shorelines of the US Atlantic Coastal
970 Plain - An improved elevation database with comparison to Earth model
971 predictions. Earth-Sci. Rev. 145, 117-131.
972 Rovere, A., Raymo, M.E., Vacchi, M., Lorscheid, T., Stocchi, P., Gómez-Pujol, L., Harris,
973 D.L., Casella, E., O'Leary, M.J., Hearty, P.J., 2016. The analysis of Last Interglacial
974 (MIS 5e) relative sea-level indicators: Reconstructing sea-level in a warmer
975 world. Earth-Science Reviews 159, 404-427.
976 https://doi.org/10.1016/j.earscirev.2016.06.006.

977 Rowlands, G. and Purkis, S., 2015. Geomorphology of shallow water coral reef
978 environments in the Red Sea. In: Rasul N. M. A. and Stewart I. C. F (eds.), the Red
979 Sea, Springer Earth System Sciences, springer-Verlag Berlin Heidelberg.
980 Rowlands, G. P., Purkis S.J., Bruckner, A.W., 2014. Diversity in the geomorphology of
981 shallow-water carbonate depositional systems in the Saudi Arabian Red Sea.
982 Geomorphology. doi:10.1016/j. geomorph.2014.03.014
983 Rust, R., Kershaw, S., 2000. Holocene tectonic uplift patterns in northeastern Sicily:
984 evidence from marine notches in coastal outcrops. Mar. Geol. 167 (1-2), 105-
985 126.
986 Schneiderwind, S., Boulton, S.J., Papanikolaou, I., Kázmér, M., Reicherter, K., 2017.
987 Numerical modeling of tidal notch sequences on rocky coasts of the
988 Mediterranean Basin. J. Geophys. Res. Earth Surf. 122, 1154–1181.
989 doi:10.1002/2016JF004132.
990 Scholz, D., Mangini, A., Felis, T., 2004. U-series dating of diagenetically altered fossil
991 reef corals. *Earth Planet. Sci. Lett*. 218, 163–178.
992 Shaked, Y., Lazar, B., Marco, S., Stein, M., Tchernov, D., Agnon, A., 2005. Evolution of
993 fringing reefs: space and time constraints from the Gulf of Aqaba. Coral Reefs
994 24. 165-172, DOI 10.1007/s00338-004-0454-2.
995 Shaked, Y., Agnon, A., Lazar, B., Marco, S., Avner, U., Stein, M., 2004. Large
996 earthquakes kill coral reefs at the north-west Gulf of Aqaba. Terra Nova 16, 133–
997 138.
998 Shaked, Y., Marco, S., Lazar, B., Stein, M., Cohen, C., Sass, E., Agnon, A., 2002. Late
999 Holocene shorelines at the Gulf of Aqaba: migrating shorelines under conditions
1000 of tectonic and sea level stability. In: EGU Stephan Mueller Special Publication
1001 Series, vol. 2 105-111.
1002 Shanas, P.R., Aboobacker, V.M., Albarakati, A.M.A., Zubier, K.M., 2017. Climate
1003 driven variability of wind in the Red Sea, Ocean Modelling 119, 105-117.
1004 http://dx.doi.org/10.1016/j.ocemod.2017.10.001.
1005 Shen, C.-C., Edwards, R.L., Cheng, H., Dorale, J.A., Thomas, R.B., Moran, S.B.,
1006 Weinstein, S., Edmonds, H.N., 2002. Uranium and thorium isotopic and
1007 concentration measurements by magnetic sector inductively coupled plasma
1008 mass spectrometry. Chem. Geol. 185, 165-178.

1009 Sofianos, S.S., Johns, W.E., 2003. An oceanic general circulation model (OGCM)
1010 investigation of the Red Sea circulation: 2. Three-dimensional circulation in the
1011 Red Sea. J. Geophys. Res. 108 (C3), 3066.
1012 Stattegger, K., Tjallingii, R., Saito, Y., Michelli, M., Thanh, N.T., Wetzel, A., 2013. Mid
1013 to late Holocene sea-level reconstruction of Southeast Vietnam using beachrock
1014 and beach-ridge deposits, *Global Planet Change* 110, 214-222.
1015 http://dx.doi.org/10.1016/j.gloplacha.2013.08.014.
1016 Stirling, C.H., Andersen, M.B., 2009. Uranium-series dating of fossil coral reefs:
1017 extending the sea-level record beyond the last glacial cycle. Earth Planet. Sci.
1018 Lett. 284, 269-283. https://doi.org/10.1016/j.epsl.2009.04.045.
1019 Stiros S.C., Pirazzoli, P.A., Fontugne, M., 2009**.** New evidence of Holocene coastal
1020 uplift in the Strophades Islets (W Hellenic Arc, Greece). Mar. Geol., 267, 207-
1021 211.
1022 Strasser, A. and Strohmenger, C., 1997. Early diagenesis in Pleistocene coral reefs,
1023 southern Sinai, Egypt: response to tectonics, sea-level and climate,
1024 Sedimentology 44, 537-558.
1025 Trenhaile, A.S., 2015. Coastal notches: their morphology, formation, and function.
1026 Earth-Science Reviews 150, 285-304.
1027 Trenhaile, A.S., Pepper, D.A., Trenhaile, R.W., Dalimonte, M., 1998. Stacks and
1028 notches at Hopewell Rocks, New Brunswick, *Canada. Earth Surf. Process. Land.*
1029 23, 975–988.
1030 Trenhaile, A.S., 1987. The Geomorphology of Rock Coasts. Oxford University Press,
1031 Oxford.
1032 Trenhaile, A.S., 1972. The shore platforms of the Vale of Glamorgan, Wales. Trans.
1033 Inst. Br. Geogr. 56, 127-144.
1034 Woodroffe, C.D. and Webster, J.M., 2014. Coral reefs and sea-level change, Mar.
1035 Geol. 352, 248-267.
1036 Wright V.P., 1994. Paleosols in shallow marine carbonate sequences, Earth Science
1037 Reviews 35, 367-395.
1038 Yokoyama, Y., Esat,T. M., Lambeck., K., 2001. Last Glacial sea-level change deduced
1039 from uplifted coral terraces of Huon Peninsula, Papua New Guinea. Quatern Int.
1040 83-85:275–283.

1041 Youssef, El. A., 1991. A note on the geomorphology of the coastal plain between Al
1042 Hudaydah and Al Salif Peninsula, Red Sea Coast, Yemen Arab Republic. The
1043 Geogr. J. 157, 71-73.
1044 Yu, K.-F., Zhao, J.-X., 2010. U-series dates of Great Barrier Reef corals suggest at least
1045 + 0.7 m sea level ~7000 years ago. The Holocene 20, 161–168.